Proceedings of the 115th European Study Group with Industry

Barcelona, January 2016

Edited by

Tim Myers, CRM
Joan Solà-Morales, UPC
Maria Aguareles, UdG
Marta Pellicer, UdG

BGSMath

MI-NET

Universitat de Girona
Càtedra Lluís A. Santaló
d'Aplicacions
de la Matemàtica

Societat
Catalana de
Matemàtiques

CRM
CENTRE DE RECERCA MATEMÀTICA

ECMI

Centre de Recerca Matemàtica
Campus de Bellaterra, Edifici C
08193 Bellaterra (Barcelona)

First edition: Juliol 2017

ISBN: 978-84-697-5163-3
Legal deposit:

Preface

The 115th European Study Group with Industry took place at the Centre de Recerca Matemática between 25-29 January, 2016.

The problems presented at the meeting were chosen to provide a wide variety of subject areas and to appeal to local academics. Specifically, the four problems concerned were:

- The manufacture of nanocrystals.
- Predicting burglaries in Catalunya.
- Equilibria in Tokamak plasmas.
- Waiting time for inventory.

Approximately 50 people attended the meeting, coming from as far afield as France and Girona. There were also participants from Ireland, Bulgaria and Georgia. Funding was primarily through the COST Action, TD1409, Mathematics for Industry Network (MI-NET) as well as the Math-In Network, the Barcelona Graduate School of Mathematics, the Catalan Maths Society and the Càtedra Lluís A. Santaló of the University of Girona.

Tim Myers, Barcelona 2016

Organising Committee

Tim Myers, Centre de Recerca Matemàtica
Joan Solà-Morales, Universitat Politècnica de Catalunya
Maria Aguareles, Universitat de Girona
Marta Pellicer, Universitat de Girona
Ernest Benedito, Universitat Politècnica de Catalunya
Àlex Haro, Universitat de Barcelona
Carlos Vázquez-Cendón, Universidade da Coruña

Contents

Synthesis of Monodisperse Spherical Nanocrystals

Problem presented by

Neus Gómez Bastús[10], Jordi Piella[10]

Report prepared by

Vincent Cregan[3,11], Revathi Bacsa[1], Marc Calvo Schwarzwälder[3], Mario Fernández-Pendás[4], Brendan Florio[6], Antonio Marquina[7], Iain Moyles[6], Tim Myers[3], Helena Ribera Ponsa[3], Simone Rusconi[4], Susana Serna[8]

Study group contributors

Revathi Bacsa[1], Wolfgang Bacsa[2], Marc Calvo Schwarzwälder[3], Vincent Cregan[3,11], Mario Fernández-Pendás[4], Sonia Fernández-Méndez[5], Brendan Florio[6], Antonio Marquina[7], Iain Moyles[6], Tim Myers[3], Helena Ribera Ponsa[3], Simone Rusconi[4], Susana Serna[8], Carlos Vázquez-Cendón[9]

Abstract: Nanoparticles, small units of matter with dimensions in the range 1-100 nm, exhibit many advantageous size-dependent magnetic, electrical, chemical and optical properties, which are not observed at the microscale or bulk. These properties are extremely sensitive to particle size, and thus the ability to produce monodisperse particles is critical. Due to its ease of use and flexibility, precipitation of nanoparticles from solution is one of

---

[1] RR Bacsa Scientific, Toulouse, France

[2] Université Paul Sabatier, Toulouse, France

[3] Centre de Recerca Matemàtica, Barcelona, Spain

[4] Basque Center for Applied Mathematics, Bilbao, Spain

[5] Universitat Politècnica de Catalunya, Barcelona, Spain

[6] MACSI, Department of Mathematics & Statistics, University of Limerick, Limerick, Ireland

[7] University of Valencia, Valencia, Spain

[8] Universitat Autònoma de Barcelona, Barcelona, Spain

[9] Universidad de A Coruña, Coruña, Spain

[10] Inorganic Nanoparticles Group, Institut Català de Nanociència i Nanotecnologia, Barcelona, Spain

[11] Report co-ordinator: vcregan@crm.cat

the most widely used synthesis methods. The main disadvantage of this method is that the relationship between particle growth and system conditions is not fully understood. In practice, the optimal reaction conditions are usually ascertained empirically or intuitively. In this report we consider several different applied mathematical techniques to explain nanoparticle growth via the precipitation method. In particular, we describe the impact of size focussing and defocussing (or Ostwald ripening) on the evolution of the nanoparticle size distribution.

1 Statement of the problem

The Inorganic Nanoparticles Group (ING) in the Institut Català de Nanociència i Nanotecnologia (Barcelona, Spain) use the precipitation from solution method to synthesise monodisperse nanoparticles. During particle growth, the concentration of the associated monomer in solution decreases as the particles grow. The resulting system of particles is not in its lowest possible energy state due to the presence of small particles. Thermodynamic equilibrium is attained by Ostwald ripening, where smaller particles dissolve due to their higher solubility, and the additional monomer is used in the growth of larger particles. However, this simultaneous growth and dissolution of bigger and smaller particles, respectively, results in the undesirable broadening of the PSD. The PSD may be refocused by changing the reaction kinetics. The main disadvantage of the precipitation method is that the exact relationship between particle growth and the system conditions is not fully understood. At present, the optimal reaction conditions are usually ascertained empirically or intuitively by the ING. Another issue is that Ostwald ripening, which is typically observed in the precipitation method, is not always observed in the ING's synthesis methods.

The Study Group was asked to address the following problems associated with the ING's nanoparticle synthesis methods.

- Can mathematical techniques be used to model and predict the evolution of the PSD?
- Why is Ostwald ripening not observed by the ING? Under which conditions will it or size focussing be observed?
- On what time scale does Ostwald ripening occur under ambient conditions?

2 Introduction

Nanotechnology is predicted to play a far reaching role in our lives in the future by impacting a variety of domains such as medicine, environmental engineering, automation, industrial production, among others. Nanoparticles are the building blocks for all these nanotechnological applications. A high surface/volume ratio is critical for most of these applications and by controlling the size, nanoparticles can be made to perform specific tasks such as drug delivery or create the much sought after tanning of the skin during controlled exposure to UV radiation. Size controlled nanoparticles find applications in medicine for targeted drug delivery, visualization including in vivo imaging, sensing, blood purification and tissue engineering [1]. Metal nanoparticles can also directly attack tumor cells by absorbing light and dissipating heat to surrounding tissue causing ablation of cancer cells. The more precise the size control, the better is the performance of the materials and for certain applications, not just size but shape and surface roughness also need to be defined precisely.

Scientists have been intensely researching viable solutions to achieve a maximum uniformity in nanoparticle morphology right at the synthesis level since these particles are so small that top down approaches used for size reduction such as grinding, etching and sieving normally are not effective. Nanoparticles can be prepared by both gas phase and solution based synthesis techniques. Both have their advantages; gas phase methods have a single formation step without the need for washing, filtering or drying. Hence, gas phase methods are particularly suited for large scale preparation [2]. Nevertheless, high temperatures are usually needed for particle production in the gas phase and not all materials have suitable precursors for gas phase crystallization. In addition, for certain applications nanoparticles need to be dispersed in appropriate solvents or in water. In such cases, controlled precipitation of the nanoparticle in the medium of choice is usually preferred. Bottom-up production of nanoparticles the liquid phase is usually carried out through controlled chemical reactions and tailoring growth conditions to ensure a self limiting self assembly of the particles.

Due to its ease of use and flexibility, precipitation of nanoparticles from solution is one of the most commonly used synthesis methods [3]. The Inorganic Nanoparticles Group (ING) in the Institut Català de Nanociència i Nanotecnologia (Barcelona, Spain) use the precipitation method to generate monodisperse gold and silver nanoparticles [4, 5]. They apply the La Mer and Dinegar synthesis strategy [6] where nucleation and growth are separated. The former of these mechanisms is used to generate seeds for particle growth. During growth, the monomer concentration decreases as the particles grow. The resulting system of varying sized particles is not in its lowest possible energy state due to the presence of small particles. Thermodynamic equilibrium is reached by size defocussing (or Ostwald ripening), where smaller particles dissolve due to their higher solubility, and the additional monomer is used in the growth of larger particles. However, this simultaneous growth and dissolution of bigger and smaller particles, respectively, results in the undesirable defocussing of the PSD. The PSD may be refocused by changing the reaction kinetics. For example, in the case of gold nanoparticles [4], the ING induced size focussing via the addition of extra monomer and adjusting the temperature and pH. However, the main disadvantage of the precipitation method is that the exact relationship between particle growth and the system conditions is not fully understood. At present, the optimal reaction conditions are usually ascertained empirically or intuitively by the ING. Another issue is that Ostwald ripening, which is typically observed in the precipitation method [7], is not observed in the ING's synthesis method.

The Study Group was asked to address the following problems associated with the ING's nanoparticle synthesis methods.

- Can mathematical techniques be used to predict the evolution of the PSD?
- Why is Ostwald ripening not observed by the ING? Under which conditions will it or size focussing be observed?
- On what time scale does Ostwald ripening occur under ambient conditions?

The outline of this report is as follows. In Section 3 we present a differential equation model for the evolution of a system of nanoparticles. Initially, we discuss the growth of single particle. The model is then extended to a system of N particles. Section 4 describes a possible mechanism as to why Ostwald ripening is not observed in the ING's synthesis method. In Section 5 a population balance equation is used to model size focussing and defocussing. Finally, in Section 6 we provide some concluding remarks and suggested directions for future work.

3 A differential equation model for nanoparticle evolution

3.1 Introduction

In this section we present a differential equation model for the evolution of a system of a nanoparticles via the mechanisms of size focussing and Ostwald ripening. Initially, we consider the growth of a single particle. The model consists of a diffusion equation for the concentration of the solution around the particle and a Stefan condition for the position of the particle surface. The Ostwald-Freundlich condition (or Gibbs-Thomson equation), which relates the particle solubility to its size, is used to obtain a boundary condition at the particle surface. Conservation of mass yields a time-dependent expression for the bulk concentration. Next, we nondimensionalise the model to obtain a small dimensionless parameter in front of the time derivative term in the diffusion equation. Exploiting the size of this parameter, we derive a pseudo-steady state concentration solution for the concentration, which is then introduced into the Stefan condition to give an ordinary differential equation (ODE) for the particle radius. The single particle model is then extended to a system of nanoparticles where each particle has its own growth equation and boundary conditions. This model is solved numerically to give the average particle size and standard deviation, both as functions of time.

3.2 Growth of a single particle

We consider a single, spherical nanoparticle, with radius r_p^*, where * denotes dimensional quantities. The schematic in Figure 1.1 shows the problem configuration. We assume that the system follows the standard La Mer model [6], whereby nucleation and growth do not occur simultaneously. Particle aggregation is also neglected. In the far-field the solution has monomer concentration c_b^*, whilst at the particle boundary the solution concentration is c_i^*. The particle solubility is denoted s^* (with the same dimensions as concentration). If the solubility $s^* < c_b^*$ then monomer molecules diffuse from the bulk towards the particle to react with the surface and the particle grows, if $s^* > c_b^*$ then the particle dissolves. To conform with standard literature (see [3, 8, 9]), we include a diffusion layer of length δ^* around the particle, where the concentration adjusts from the c_i^* to c_b^*.

The monomer concentration is modelled via the diffusion equation

$$\frac{\partial c^*}{\partial t^*} = \frac{D}{r^{*2}} \frac{\partial^*}{\partial r^*} \left(r^{*2} \frac{\partial c^*}{\partial r^*} \right) , \tag{1}$$

where c^* is the concentration, r^* is the distance from the centre of the particle, t^* is time and D is the diffusion coefficient. The associated boundary and initial conditions are

$$c^*(r_p^*, t^*) = c_i^* , \qquad c^*(\delta^*, t^*) = c_b^*(t^*) , \qquad c^*(r^*, 0) = c_{b0}^* \quad \text{for } r^* > r_p^* \ , \tag{2}$$

where the condition at $t^* = 0$ states that initially the monomer solution is well-mixed and at a uniform concentration, c_{b0}^*.

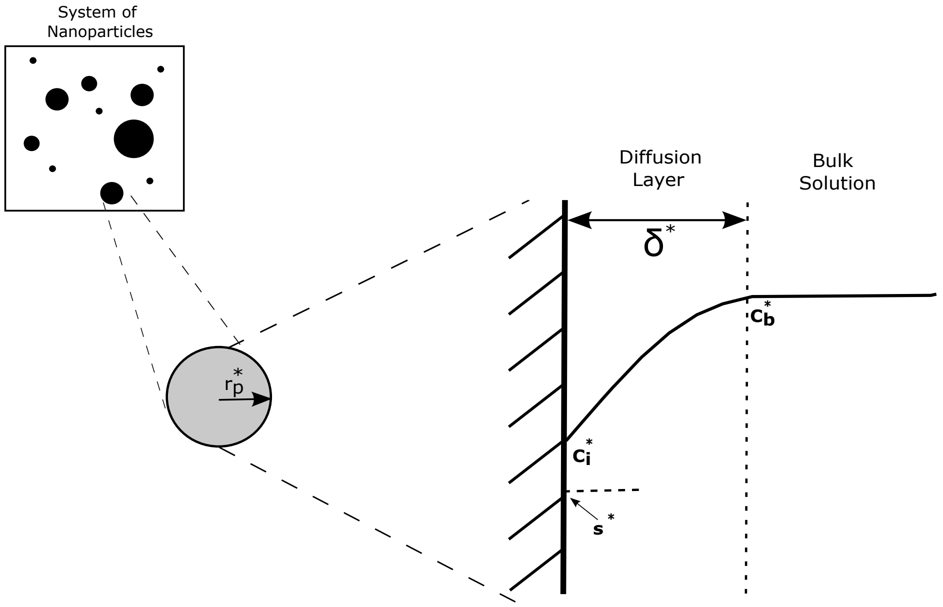

Figure 1.1: Schematic of nanoparticles in solution with a close-up of a single nanoparticle with radius r_p^* and the surrounding monomer concentration profile where s^*, c_i^* and c_b^* are the particle solubility, the concentration at the surface of the particle and the far-field concentration, respectively [8].

In practice the particle surface concentration, c_i^*, is difficult to measure [8]. Thus, we eliminate it from the model by considering two equivalent expressions for the mass flux at the particle surface, J. Firstly, Fick's first law states that the flux of monomers passing through a spherical surface of radius r^* is

$$J = 4\pi r^{*2} D \frac{\partial c^*}{\partial r^*} \,. \tag{3}$$

The flux is also given by the first-order reaction expression

$$J = 4\pi r^{*2} k (c_i^* - s^*) \,, \tag{4}$$

where k is a rate constant. Equating (3) with (4) gives

$$c_i^* = s^* + \frac{D}{k} \frac{\partial c^*}{\partial r^*}\bigg|_{r^*=r_p^*} \,, \tag{5}$$

which defines the concentration c_i^* for the surface condition of (2).

The particle solubility, s^*, is given by the OFC

$$s^* = s_\infty^* \exp\left(\frac{2\sigma V_M}{r_p^* R_G T}\right) \equiv s_\infty^* \exp\left(\frac{\alpha}{r_p^*}\right) , \tag{6}$$

where s_∞^* is the solubility of the bulk material (i.e., with zero curvature), σ the interfacial energy, V_M is the molar volume of monomer in solution, R_G the universal gas constant, T the absolute temperature and $\alpha = (2\sigma V_M)/(R_G T)$ the capillary length. This equation shows that the particle solubility increases as particle size decreases. The fact that smaller particles are more soluble than larger ones is the basis of Ostwald ripening. The capillary length, α, defines the length scale below which curvature-induced solubility is significant.

The diffusion equation is solved on a domain $r^* > r_p^*$, where the particle radius is an unknown function of time. To determine the radius we consider the change in volume of a particle

$$\frac{d}{dt^*}\left(\frac{4}{3}\pi r_p^{*3}\right) = 4\pi r_p^{*2}\frac{\mathrm{d}r_p^*}{\mathrm{d}t^*} = V_M J\,. \tag{7}$$

Substituting for J via (3) leads to

$$\frac{\mathrm{d}r_p^*}{\mathrm{d}t^*} = V_M D\left.\frac{\partial c^*}{\partial r^*}\right|_{r^*=r_p^*}, \qquad r_p^*(0) = r_{p0}^*\,, \tag{8}$$

where r_{p0}^* is the initial particle radius.

Finally, to complete the system we require an expression for the time-dependent bulk concentration, $c_b^*(t^*)$. If we have consider the particle in a given volume of liquid $V = 4\pi R^3/3$, then mass conservation of the monomer atoms in the particle and surrounding solution requires that

$$\frac{4\pi}{3}\left[\rho_p r_{p0}^{*3} + M_p c_{b0}^*(R^3 - r_{p0}^{*3})\right] = \frac{4\pi}{3}\left[\rho_p r_p^{*3} + M_p c_b^*(t)(R^3 - r_p^{*3})\right], \tag{9}$$

where ρ_p is density and M_p is molar mass. Rearranging (9) leads to

$$c_b^*(t) = c_{b0}^*\left(\frac{R^3 - r_{p0}^{*3}}{R^3 - r_p^{*3}}\right) + \frac{\rho_p}{M_p}\left(\frac{r_{p0}^{*3} - r_p^{*3}}{R^3 - r_p^{*3}}\right). \tag{10}$$

Nondimensionalisation

The model is nondimensionalised via the change of variables

$$r = \frac{r^*}{r_{p0}^*}\,, \qquad r_p = \frac{r_p^*}{r_{p0}^*}\,, \qquad t = \frac{t^*}{\tau^*}\,, \qquad c = \frac{c^* - s_0^*}{\Delta c}\,, \qquad c_b = \frac{c_b^* - s_0^*}{\Delta c}\,, \tag{11}$$

where $\Delta c = c_{b0}^* - s_0^*$ represents the driving force for particle growth and $s_0^* = s_\infty^* \exp(\alpha/r_{p0}^*)$ is the initial particle solubility. The solubility is scaled in the same way as the concentration. The concentration and growth equations yield two possible time scales $\tau_D^* \sim r_{p0}^{*2}/D$ and $\tau_R^* \sim r_{p0}^{*2}/(V_M D\Delta c)$, respectively. To focus on the particle growth we choose the growth time scale $\tau^* = \tau_R^*$.

The governing system consisting of (1), (2), (5), (8) and (10) is now transformed to

$$\epsilon\frac{\partial c}{\partial t} = \frac{1}{r^2}\frac{\partial}{\partial r}\left(r^2\frac{\partial c}{\partial r}\right), \qquad \frac{\mathrm{d}r_p}{\mathrm{d}t} = \left.\frac{\partial c}{\partial r}\right|_{r=r_p}, \tag{12}$$

$$c(r_p, t) = s + Da\left.\frac{\partial c}{\partial r}\right|_{r=r_p}, \qquad c(\delta, t) = c_b(t)\,, \qquad c(r, 0) = 1\,, \qquad r_p(0) = 1\,, \tag{13}$$

$$c_b(t) = -s_0 + c_{b0}\left(\frac{\beta - 1}{\beta - r_p^3}\right) + c_1\left(\frac{1 - r_p^3}{\beta - r_p^3}\right), \tag{14}$$

where

$$s = s_\infty \exp\left(\omega/r_p\right) - s_0\,, \tag{15}$$

and

$$\epsilon = V_M \Delta c\,, \qquad \delta = \frac{\delta^*}{r^*_{p0}}\,, \qquad Da = \frac{D}{k r^*_{p0}}\,, \qquad \omega = \frac{\alpha}{r^*_{p0}}\,, \qquad s_\infty = \frac{s^*_\infty}{\Delta c}\,, \tag{16}$$

$$s_0 = \frac{s^*_0}{\Delta c}\,, \qquad c_{b0} = \frac{c^*_{b0}}{\Delta c}\,, \qquad c_1 = \frac{\rho_p}{M_p \Delta c}\,, \qquad \beta = \frac{R^{*3}}{r^{*3}_{p0}}\,. \tag{17}$$

The above system contains several dimensionless parameters. The first, ϵ, is typically very small. For example, Talaplin *et al.*, [10] studied cadmium selenide (CdSe) nanoparticles with initial radii in the range $1 - 100\,\text{nm}$, with a capillary length of 1.6nm and a solution with $c^*_b = 15 s^*_\infty$ so that $\epsilon = \mathcal{O}(10^{-6})$. Physically, this suggests that growth is orders of magnitude slower than the diffusion time scale, that is, the concentration adjusts much faster than growth occurs and so the system can be considered as pseudo-steady. Thus, the time derivative can be omitted from the concentration equation. However, since time also enters into the problem through the definitions of r_p and c_b this is not a true steady-state situation. The parameter Da is an inverse Damköhler number measuring the relative magnitudes of diffusion to surface reactions [3].

Pseudo-steady state solution

As ϵ is typically much smaller than one, we neglect the time derivative in the diffusion equation and obtain the pseudo-steady state approximation [3, 11, 12, 13]

$$\frac{1}{r^2}\frac{\partial}{\partial r}\left(r^2 \frac{\partial c}{\partial r}\right) = 0\,. \tag{18}$$

Upon integrating and applying the boundary conditions we obtain

$$c = -\frac{A}{r} + B\,, \tag{19}$$

where

$$A = \frac{\delta r_p^2 (s - c_b)}{r_p(r_p - \delta) - \delta Da}\,, \qquad B = s + A\left(\frac{1}{r_p} + \frac{Da}{r_p}\right)\,. \tag{20}$$

Numerous authors [8, 10, 14] have observed that $r_p \ll \delta$. Exploiting this relation (20) reduces to

$$A = \frac{r_p^2 (c_b - s)}{Da + r_p}\,, \qquad B = c_b\,. \tag{21}$$

Substituting this solution for the concentration into the Stefan condition in (12) leads to

$$\frac{\mathrm{d}r_p}{\mathrm{d}t} = \frac{c_b - s}{Da + r_p} = \frac{c_b + s_0 - s_\infty \exp(\omega/r_p)}{Da + r_p}\,, \tag{22}$$

where c_b is defined in terms of r_p by equation (14). The problem is now reduced to the solution of a single first-order ODE for r_p which can be solved numerically.

3.3 Evolution of a system of N particles

The single particle model is now extended to a system of N particles that follow a standard normal distribution with mean initial radius $\overline{r}_{p0}^*$ and standard deviation σ_o. The particle radii, initial radii and solubilities are denoted r_{pi}^*, $r_{pi,0}^*$ and s_i^*, respectively, where i represents the i^{th} particle and $i = 1, \ldots, N$. We nondimensionalise via (11) with the only difference being that the length scale r_{p0}^* is replaced with the mean value $\overline{r}_{p0}^*$. This also changes the concentration scale, Δc, in that s_0^* is defined in terms of the mean value $\overline{r}_{p0}^*$. Hence, all overlined dimensionless parameters are the same as those defined in (16) and (17), except r_{p0}^* is replaced by $\overline{r}_{p0}^*$.

Under the pseudo-steady approximation the growth of each particle is now described by an equation of the form (22), except r_p, s_0 are replaced by the values r_{pi}, s_{0i}. The bulk concentration equation must account for all particles, and thus

$$c_b^*(t^*) = c_{b0}^* \left(\frac{R^3 - \sum\limits_{i=1}^{N} r_{p0}^{*3}}{R^3 - \sum\limits_{i=1}^{N} r_{pi}^{*3}} \right) + \frac{\rho_p}{M_p} \left(\frac{\sum\limits_{i=1}^{N} r_{p0}^{*3} - \sum\limits_{i=1}^{N} r_{pi}^{*3}}{R^3 - \sum\limits_{i=1}^{N} r_{pi}^{*3}} \right). \tag{23}$$

In dimensionless form the problem is then governed by

$$c_b(t) = -\overline{s_0} + \overline{c}_{b0} \left(\frac{R^3 - \sum\limits_{i=1}^{N} r_{p0}^{*3}}{R^3 - \overline{r}_p^3 \sum\limits_{i=1}^{N} r_{pi}^3} \right) + \overline{c}_1 \left(\frac{\sum\limits_{i=1}^{N} r_{p0}^{*3} - \overline{r}_p^3 \sum\limits_{i=1}^{N} r_{pi}^3}{R^3 - \overline{r}_p^3 \sum\limits_{i=1}^{N} r_{pi}^3} \right), \tag{24}$$

and

$$\frac{\mathrm{d}r_{pi}}{\mathrm{d}t} = \frac{c_b - \overline{s}}{\overline{Da} + r_{pi}} = \frac{c_b + \overline{s}_0 - \overline{s}_\infty \exp(\overline{\omega}/r_{pi})}{\overline{Da} + r_{pi}}. \tag{25}$$

A finite difference numerical scheme is used to solve the above system of equations. A brief overview of the the numerical scheme and the associated pseudocode is given Appendix A.1.

3.4 Results

In this section we describe the numerical results and validate the model by comparing it with experimental data. Specifically, we use data from the highly cited experimental study of Peng *et al.*, [7] for the growth of cadmium selenide (CdSe) nanoparticles. One of the major challenges in developing an accurate theoretical description for nanoparticle growth via solution is the lack of appropriate experimental data. Clark *et al.*, [15] note the scarcity of data for the production of monodisperse nanocrystals, and the inherent difficulty in measuring particle concentrations, especially at the nanoscale. We apply a similar approach used by previous treatments *et al.*, [3, 15] where the unknown parameters are used as fitting parameters. For the present analysis, four values are unknown: the reaction rate k, the bulk solubility s_∞^*, the initial monomer concentration c_{b0}^* and the volume of liquid surrounding a particle, V. We perform a parameter sweep for the above values until we obtain the best fit between the model and the data. The main parameter values are listed in Table 1.1, and those in italics were obtained via the parameter sweep method.

Quantity	Symbol	Value	Units
Universal gas constant	R_G	8.31446	$\mathrm{J\,mol^{-1}\,K^{-1}}$
Density	ρ_p	5816	$\mathrm{kg\,m^{-3}}$
Molar volume	V_M	3.29×10^{-5}	$\mathrm{m^3\,mol^{-1}}$
Molar mass	M_p	0.1914	$\mathrm{kg\,mol^{-1}}$
Solution temperature	T	573.15	K
Surface energy	σ	0.44	$\mathrm{J\,m^{-2}}$ [16]
Capillary length	α	6×10^{-9}	m
Diffusion coefficient	D	10^{-9}	$\mathrm{m^2\,s^{-1}}$
Reaction rate	k	0.8797	$\mathrm{m\,s^{-1}}$
Solubility of bulk material	s^*_∞	1.64×10^{-9}	$\mathrm{mol\,m^{-3}}$
Initial bulk concentration	c^*_{b0}	9.46×10^{-7}	$\mathrm{mol\,m^{-3}}$
Volume of liquid around particles	V	5.57×10^{-12}	$\mathrm{m^3}$

Table 1.1: Physical parameters for the cadmium selenide (CdSe) nanoparticle synthesis method used by Peng *et al.*, [7]. The parameters in italics were obtained via a model fitting approach.

Figure 1.2(a) shows the growth of a CdSe particle with an initial radius of 2 nm. The bulk concentration (red line) and particle solubility (black line) are shown in Figure 1.2(b). We selected a bulk concentration higher than the particle solubility, which causes the particle to grow. We chose a relatively small surrounding fluid volume, so that monomer is rapidly consumed. Growth ends close to 2000 s, when the particle radius is approximately 3 nm. The concentration curves show that the growth stopping corresponds to the time the two curves overlap (theoretically the curves asymptote towards each other and growth continues at an ever diminishing rate).

Of course, for a single particle size focussing or defocussing cannot be observed. To illustrate these phenomenona, in Figure 1.3 we show the evolution of two CdSe nanoparticles, with initial radii of 3.5 and 5 nm. The change in radii is shown in Figure 1.3(a) where the red and blue lines denote the 3.5 nm and 5 nm particles, respectively. The inset shows the absolute difference in radii for the first 1500 s. As before we choose the bulk concentration higher than both particle's solubility leading to an initial rapid growth phase. However, the monomer quickly depletes and after approximately 300 s the process changes. The growth rate for the larger particle slows down, but it still continues to grow for the remainder of the simulation. Meanwhile the smaller particle starts to slowly dissolve and the rate of dissolution increases with time. The inset figure, showing $|r^*_{p1} - r^*_{p2}|$, demonstrates that initially size focussing occurs but beyond 400 s the radii diverge and there is defocussing. Figure 1.3(b) shows the bulk concentration (black line), and the solubilities of the 3.5 nm (red line) and 5 nm (blue line) particles. Initially, the solubility of both particles is well below the bulk concentration and so the particles grow. As a result the bulk concentration rapidly decreases. The smaller particle stops growing at around 700 s corresponding to a change in the solubility slope. However, at this time both particles still have a solubility below that of the bulk. So the larger particle is gaining monomer from the smaller particle before the bulk monomer is used up, i.e.,

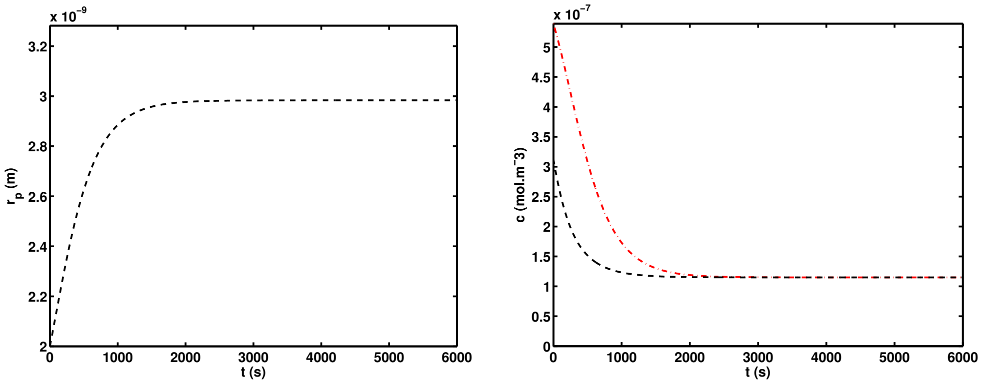

(a) (b)

Figure 1.2: (a) Radius of a CdSe nanoparticle with initial radius 2 nm and (b) associated bulk concentration (red line) and particle solubility (black line). $V = 5.57 \times 10^{-15}\mathrm{m}^3$.

Ostwald ripening occurs even when there is sufficient monomer in the solution for both particles to grow. Shortly after 1000 s the smaller particle's solubility increases above that of the bulk and keeps on increasing until the end of the computation. The larger particle has a slowly decreasing solubility, in keeping with its slow growth, which always remains below the bulk concentration (although once the smaller particle disappears the growth will eventually stop). When compared to the one particle figures it is clear that Ostwald ripening is a significantly slower process relative to simple growth.

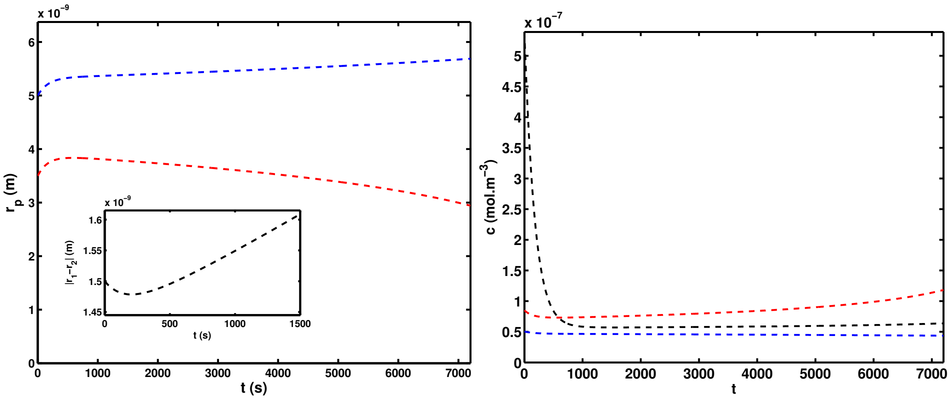

(a) (b)

Figure 1.3: Evolution of two CdSe nanoparticles. (a) Radii of particles with initial radii of 3.5 nm (red line) and 5 nm (blue line). The inset is a zoom-in of the absolute difference in the particle radii near the beginning of the process. (b) Change in bulk concentration (black line) and solubilities of smaller (red line) and larger (blue line) particles. $V = 1.1 \times 10^{-14}\mathrm{m}^3$.

Figure 1.4 compares our simulation of an evolving system of 1000 CdSe particles (red lines) with the corresponding data of Peng *et al.*, [7] (black lines). Figure 1.4 shows the change in average particle radius, $\overline{r_p}$, and standard deviation percentage, $\sigma_{o,\%}$. Once particles go below a radius threshold of 1.5 nm, they are no longer considered when computing $\overline{r_p}$ and $\sigma_{o,\%}$. The initial average radius and standard deviation percentage are 2.1 nm and 20%, respectively. The solution captures the main qualitative features of the growth process. At the beginning of the process, the concentration in the solution is higher than the solubility of all the particles. Thus, the particles consume material in the solution and grow, leading to an increase in $\overline{r_p}$. As the growth rate of the small particles is larger than that of the bigger particles, size focussing occurs as indicated by the rapid decrease in $\sigma_{o,\%}$. Particle growth results in the depletion of material from the solution, and hence a decrease in the concentration. Eventually, the solubility of the smaller particles drops below the bulk concentration. Consequently, they start to dissolve, whilst bigger particles continue to grow. This defocussing is observed after approximately one hour where $\sigma_{o,\%}$ begins to gradually increase. After approximately 3 hours, additional precursors are added to the solution, which leads to a rapid decrease in $\sigma_{o,\%}$, and thus the slow broadening of the PSD.

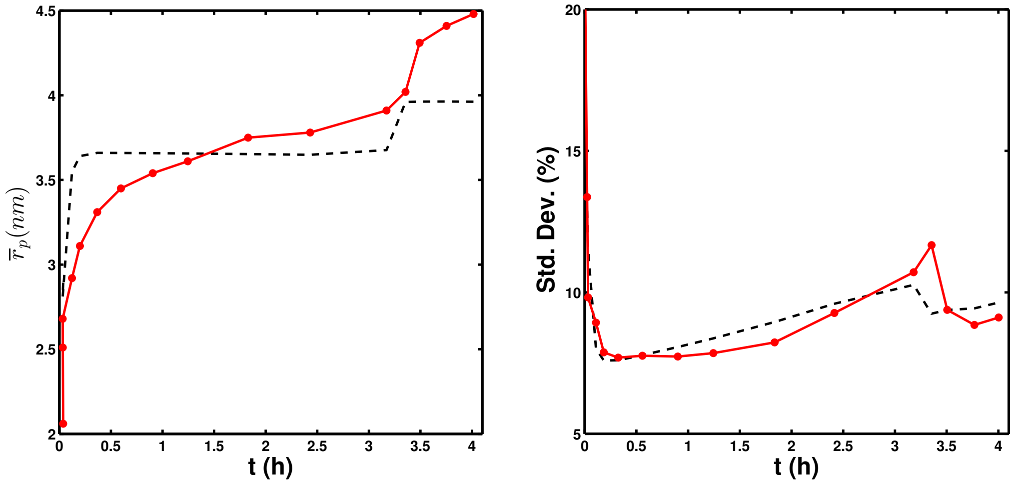

(a) (b)

Figure 1.4: Results of numerical simulation (black line) for (a) average particle radius and (b) standard deviation (%) compared to corresponding experimental data (red line) [7] for a system of 1000 CdSe nanoparticles. $V = 5.57 \times 10^{-12} \mathrm{m}^3$.

3.5 Conclusions

In this section we presented an ODE model for nanoparticle growth via the precipitation method. In particular, we simulated the evolution of a system of 1000 CdSe nanoparticles. The numerical results captured the processes of size focussing and Ostwald ripening. Moreover, the results showed good qualitative agreement with the corresponding experimental data of Peng *et al.*, [7].

As discussed, we considered the growth of CdSe particles as most of the parameter values were readily available. However, we still had to use a parameter sweep routine to obtain four unknown parameters. Previous studies [15] have encountered similar issues in finding suitable parameters. One of our future tasks will be to liaise closely with the IGN and find the correct parameters for their synthesis methods. This may involve creating experiments that can be used to obtain specific parameter values.

4 A model for Ostwald ripening

The most important factor in determining the size evolution of particles nucleating or growing in a solvent is the difference between bulk concentration of some precipitating substance (monomer) and the solubility of the particle that is growing or shrinking. When a particle's solubility, based on its current size, is exceeded by the bulk concentration of monomer then the particle will grow. Conversely, if the particle's solubility is greater than the bulk concentration, it will shrink and release monomer back into the solvent. The solubility of a particle is determined by its chemical potential, a thermodynamic quantity which relates the Gibbs energy of the system to the number of moles of the precipitating particle. At the nanoscale, the curvature of the nanoparticle surface becomes significant enough to affect the particle's solubility. As highlighted in Section 3, the solubility is described by the Gibbs-Thomson equation

$$s(r_p) = s_\infty \exp\left(\frac{\mu_1}{RT}\right), \tag{26}$$

where

$$\mu_1 = \frac{2\sigma V_M}{r_p}.$$

We recall that s_∞ is the bulk solubility, σ is the particle-solvent surface tension, V_M is the molar volume of the precipitate, R is the universal gas constant, T is the temperature and r_p is the radius of the particle. We note that the dimensional * notation has been neglected. From this expression we can see that as r_p becomes large, the size-dependent solubility approaches the bulk value. A full model of the precipitation dynamics must take into account the diffusion of the monomer in the solution; however, as diffusion occurs on a fast timescale, the growth of the radius of the i-th particle may be approximated by

$$\frac{\mathrm{d}r_{pi}}{\mathrm{d}t} = \frac{k\big(c_b - c_{ei}(r_p)\big)}{r_p}, \tag{27}$$

where k is the mass transfer coefficient, c_b is the concentration of monomer and $c_{ei}(r_p)$ is the particle solubility defined by (26) for the i-th particle.

In Figure 1.5, we illustrate two particle dynamics using a standard Gibbs-Thomson solubility model defined in (26). We see that initially at some time t_0, both particles have a solubility below the bulk concentration and so both particles grow according to (27) (Figure 1.5(a)). By conservation of mass, if there is no external source of the monomer then the bulk concentration also decreases. As small particles have a faster growth rate, the size of the particles move closer together and the size distribution is said to be focussing. At some new time t_1, one particle is in equilibrium with the bulk concentration while the other particle is still below. The first particle remains at rest while the second particle grows because of the concentration difference. Since one particle is still growing, the

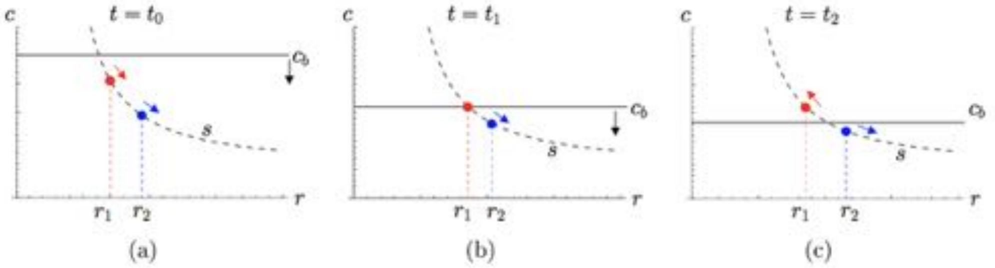

Figure 1.5: The particle solubility as a function of size for a two particle system. Particles must lie on the dashed curve defined by (26), and the bulk concentration is shown for reference. As time progresses the sizes of the two particles diverge.

bulk concentration decreases further (Figure 1.5(b)). Finally at some other time t_2, the first particle, which was previously stationary, now has a solubility higher than the bulk concentration and as a consequence, shrinks. The second, larger particle, still exists below the bulk threshold and continues to grow (Figure 1.5(c)). Ultimately, larger particles grow at the expense of smaller ones i.e., Ostwald ripening. The key to this size defocussing mechanism is that (26) is monotonically decreasing in size; that is, growing particles never increase their solubility. As long as a solubility curve defined in (26) is used, the dynamics explained will continue to happen and Ostwald ripening will occur. Ostwald ripening can be controlled by constantly injecting monomer into the system to ensure the bulk concentration, c_b, remains above the solubility of the small particles. That is, if the right-hand side of (27) remains positive for all particles then only growth occurs so there is no defocussing behaviour as in Ostwald ripening.

The ING have noticed that Ostwald ripening may not occur for gold nanoparticles without monomer injection. As the Gibbs-Thomson model predicts Ostwald ripening must occur, there is some aspect of the physics that the model is failing to capture.

4.1 Binary mixtures, emulsions and inhibition of Ostwald ripening

An important property of nanoparticles is their ability to remain suspended in solution as a result of their high surface area, which allows them to bond with sufficient strength to the solvent so as to overcome differences in density. However, in the suspended state, nanoparticles are also subjected to inter-particle forces and tend to coalesce into the bulk state that has a lower surface energy, and hence is thermodynamically more stable. Particle-particle forces include weak Van der Waals forces, stronger polar and electrostatic interactions or covalent interactions. Depending on the viscosity and polarisability of the fluid, particle aggregation is determined by the interparticle interaction. Hence, surfactants are used to coat nanoparticle surfaces to change the nature of the interparticle interaction and prevent coalescence. The balance between particle interaction forces and particle – fluid interactions is of vital importance to describe the temporal evolution of free particles.

In discussions with the ING as to possible mechanisms that could explain the inhibition of Ostwald ripening, we were alerted that the gold nanoparticles are citrate stabilized:

citrate is added to the solvent to form a monolayer coating around the particles to prevent collisions between adjacent particles, and to reduce the dissolved ionic gold to particulate elemental gold (Figure 1.6). An example of a possible reaction pathway for this to happen is presented in Figure 1.7 reproduced from [17]. In this reaction chloroauric acid dissociates and reacts with citrate to produce a gold-chlorine-citrate ionic complex. Secondary reactions occur (step b in Figure 1.7) and one of the principal products that forms is $AuCl_2^-$. The significance of this product is the transformation of the gold complex from Au^{3+} to Au^{1+}. The final stage of the reaction is to produce solid gold particles and to transform the gold complex back into Au^{3+} and reform chloroauric acid. The formation of gold nanoparticles is therefore a complex cascade of chemical reactions but for the purpose of modelling we will consider a simpler solution of gold ions which precipitate to gold particles and citrate ions which help stabilize the particle.

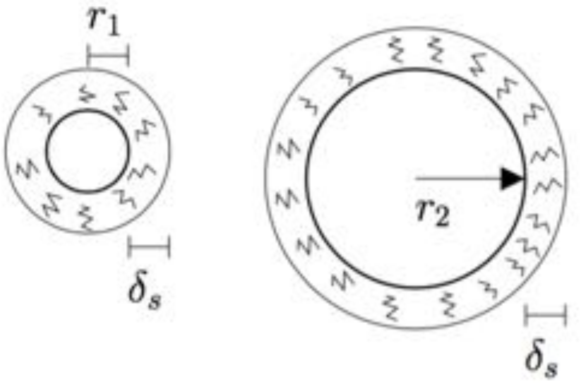

Figure 1.6: As the gold nanoparticles form, citrate forms a monolayer by physisorption to the particle surface. Further layer thickness is generally prohibited due to the negative charge of citrate repelling loose citrate molecules.

By adding a secondary material to coat the nanoparticle, it was considered that single material thermodynamic theory would no longer be correct for describing a binary gold/citrate particle. Such a consideration was already found in the studies of emulsions; solvents with small droplets of non-soluble liquids dispersed within demonstrated an ability to stop Ostwald ripening. In an emulsion system, along with insoluble droplets, there is a solvent and disperse phase which can exchange mass in a way that leads to Ostwald ripening. However, by adding the secondary component which cannot transfer mass with the solvent due to its insolubility, the chemical equilibrium is drastically altered. The chemical potential of the system must remain in equilibrium but since the solvent and insoluble component cannot interact, the disperse solute phase must compensate for this. The chemical potential is then defined by

$$\mu_1 = \frac{2\sigma V_M}{r_p} + RT\log(\gamma x_1), \tag{28}$$

where x_1 is the molar fraction of gold and γ is the activity coefficient of gold in the mixture.

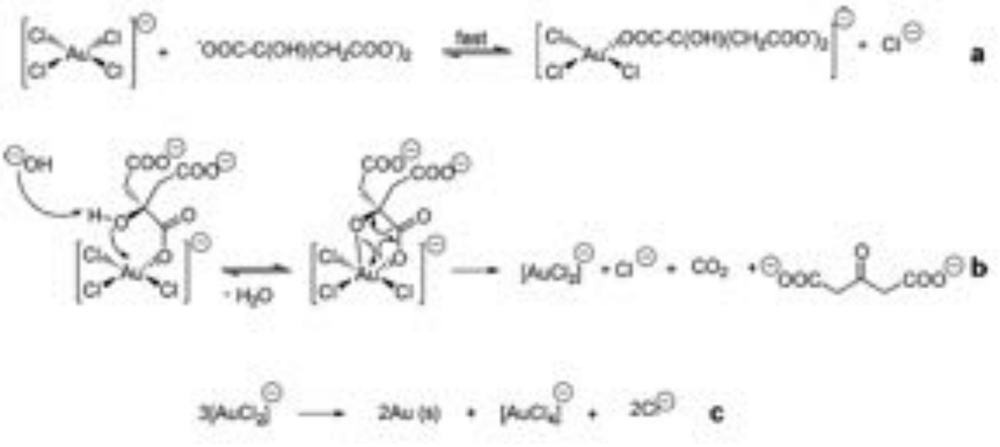

Figure 1.7: An example reaction of gold nanoparticle formation with citrate. The figure is reproduced from [17].

The mixture is binary with citrate so we have

$$x_1 + x_2 = 1,$$

where x_2 is the molar fraction of citrate. It is important to remark that by considering mole fractions of each component, we are not accurately representing a discrete gold-citrate layer as depicted in Figure 1.6 but rather making the simplification of gold and citrate coexisting in a binary liquid. We make this simplification to outline the significant role a second substance can have on the mixture potential and leave modelling of the truly distinct phases for future work. Making this assumption, the number of moles of each constituent, j, is given by

$$n_j = v_j \frac{\rho_j}{M_{pj}}, \tag{29}$$

where v is the volume, ρ is the density and M_p is the molar mass. The volume of the spherical gold nanoparticle is given by[1]

$$v_1 = \frac{4\pi}{3} r_p^3, \tag{30}$$

whereas the volume of the citrate is

$$v_2 = \frac{4\pi}{3}\big((r_p + s)^3 - r_p^3\big), \tag{31}$$

where s is the thickness of the citrate monolayer which we take to be approximately 1 nm. Now we can calculate the molar fraction of the particle by using

$$x_1 = \frac{n_1}{n_1 + n_2}, \tag{32}$$

---

[1] Once again we emphasize that since we're applying the molar fraction on a binary mixture, we cannot state with certainty that the central particle is entirely gold and the outer layer entirely citrate but we assume this discrete layer formulation provides a representative volume of each component.

to find that

$$x_1 = \left[1 + \beta\left(\frac{(r+s)^3}{r^3} - 1\right)\right]^{-1}, \tag{33}$$

where

$$\beta = \frac{\rho_2 M_1}{\rho_1 M_2}.$$

The solubility of the particle then becomes

$$c_e(r_p) = c_\infty \gamma x_1 \exp\left(\frac{\alpha}{r_p}\right), \qquad \alpha = \frac{2\sigma V_M}{RT}. \tag{34}$$

One immediate noticeable change is that the monotonicity of the solubility is no longer true and solubility can increase for increasing particle size.

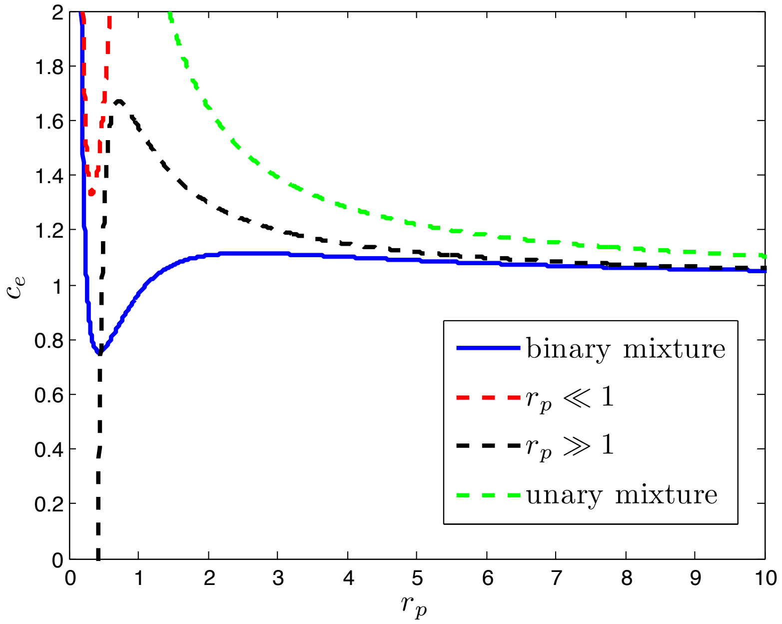

Figure 1.8: Solubility expressions against particle radius. The blue curve is a representative profile of (34) with the parameter set $\beta = 0.07$, $\alpha = 1$, $\gamma = 1$, and $s = 2$. The red curve, black curve, and green curve represent the small r_p, large r_p, and original solubility curve respectively.

Figure 1.8 shows an example profile for (34) with the parameter set $\beta = 0.07$, $\alpha = 1$, $\gamma = 1$, and $s = 2$. Indeed we see that the monotonicity is broken. Plotted alongside (34) are the small r_p asymptotics (red curve), large r_p asymptotics (black curve), and the previous monotonic solubility curve (green). The asymptotic limits for (34) are

$$c_e \sim c_\infty \frac{\gamma\beta}{s^3} r_p^3 \exp\left(\frac{\alpha}{r_p}\right), \qquad r_p \ll 1, \tag{35a}$$

$$c_e \sim c_\infty \gamma \left(1 - \frac{3\beta s}{r_p}\right) \exp\left(\frac{\alpha}{r_p}\right), \qquad r_p \gg 1. \tag{35b}$$

We notice that as r_p increases we approximate the original monotonic solubility curve (scaled by the activity coefficient). This follows logically from the restriction that the citrate volume is effectively concentrated in the monolayer. As the particle size increases, the extra volume attributed to the citrate is minimal and the particles would behave as if the citrate coating was not present. However, it is worth noting that the second order correction in (35b) produces a negative term which means that as β gets large, the solubility curve will have a positive slope and approach the asymptotic limit from below. This means that the gradient with the bulk value will be larger than in the citrate free case and this could alter the particle dynamics. It is worth investigating if such a system is chemically plausible. In the small r_p limit we see that an effective potential well forms which captures the ability for particles to stabilize in size. In Figure 1.9 we illustrate the mechanism for this stabilized growth.

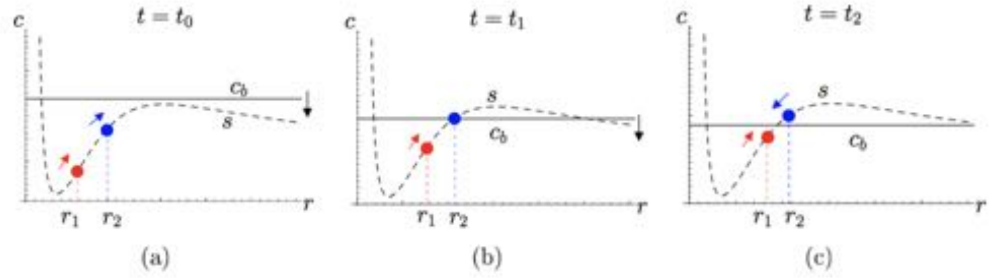

Figure 1.9: The particle solubility as a function of size for a two particle system. Particles must lie on the modified solubility profile (dashed), and the bulk concentration is shown for reference. As time progresses the sizes of the two particles converge and Ostwald ripening is not occurring.

We see, like before, that initially at some time t_0, both particles have a solubility below the bulk concentration and so both particles grow (Figure 1.9(a)). Small particles grow faster so the size distribution is focussing. At some new time t_1, one particle is in equilibrium with the bulk concentration while the other particle is still below. Unlike the Gibbs-Thomson solubility theory, the equilibrium particle is the larger particle. The smaller particle grows because of the concentration difference (Figure 1.9(b)). Finally at some other time t_2, the larger particle has a solubility higher than the bulk concentration and as a consequence, shrinks. The smaller particle still exists below the bulk threshold and grows (Figure 1.9(c)). Since the growth rate is proportional to the difference between bulk concentration and solubility, the bulk value can never be smaller than the solubility of the smaller particle. As a consequence, both particles move towards the same size; Ostwald ripening is not occurring here as the particles size distribution is and will remain focussing. This is a result of the particular form of solubility curve shown in Figure 1.9 and the initial location of particles on the curve. If there are particularly large particles on the decreasing part of the curve, Ostwald ripening can still occur, though some small particles may reach an equilibrium size resulting in a bidisperse distribution. Unlike the Gibbs-Thomson theory which can only change solubility by global parameters such as temperature, the new solubility model allows for more local parameter adjustments such as the thickness of the monolayer around the nanoparticle and the chemical properties of the stabilizing agent (citrate).

4.2 Conclusions

After considering a new model of solubility, it is worth conducting some experiments to validate some of the hypotheses. In particular, it is worthwhile to investigate how the amount of citrate used affects the particle size distribution. It might also be fruitful to experiment with other stabilizing agents to see if Ostwald ripening is still inhibited. It is worth investigating the inhibition of Ostwald ripening in terms of particle sizes relative to the thickness of the monolayer created by the stabilizing agent. If the stabilizing agent forms a constant thickness then this would effectively monitor the changing molar fraction on the ripening process. As particles get bigger, the effect of the molar fraction would decrease and ripening should occur again. Separating distributions of particle sizes where Ostwald ripening is occurring and where it is inhibited can help develop the model further.

5 Population balance equation approach

Population Balance Equation (PBE) models have been frequently used to describe processes such as crystallization, polydisperse solids dissolution and nanoparticle synthesis. The advantages of the PBE approach have been widely explored before [18, 19, 20]. In this section we propose a general PBE model for the kinetics of spherical nanoparticle synthesis.

5.1 A general model

We first define a distribution $n(r,t)$ such that the integral

$$\int_{\alpha}^{\beta} n(r,t)\ \mathrm{d}r\,, \tag{36}$$

corresponds to the expected number of spherical particles with radius $r \in [\alpha, \beta]$, for any given time t. The density, $n(r,t)$, is the particle size distribution (PSD), and our aim is to model its evolution with time. More precisely, one can derive a PBE which accounts for the different mechanisms that drive the dynamics of $n(r,t)$.

The growth function, $g(r,t)$, is defined to be the expected variation of radius r with respect to time t that models the particles growth. Thus,

$$\frac{\mathrm{d}r}{\mathrm{d}t} = g(r,t). \tag{37}$$

We also define $k_n(r,t)$ to be the rate of nucleated particles with radius r for any time t such that

$$\int_{\alpha}^{\beta} k_n(r,t)\ \mathrm{d}r\,, \tag{38}$$

provides the expected number of new nucleated particles per unit time. Finally, Ostwald ripening is modelled via the rate function $k_d(r,t)$ such that

$$\int_{\alpha}^{\beta} k_d(r,t)\, n(r,t)\ \mathrm{d}r\,, \tag{39}$$

yields the expected number of particles dissolving back into solution per unit time.

The PBE driving the evolution of $n(r,t)$ is formulated by accounting for the above processes and their corresponding functions $g(r,t)$, $k_n(r,t)$ and $k_d(r,t)$. If we consider an infinitesimal rectangle $[r, r+dr] \times [t, t+dt]$, the population balance equation for the expected number of particles with radius $x \in [r, r+dr]$ during the time interval $[t, t+dt]$:

$$\begin{aligned}
&\underbrace{\int_r^{r+\mathrm{d}r} n(x, t+\mathrm{d}t)\ \mathrm{d}x - \int_r^{r+\mathrm{d}r} n(x,t)\ \mathrm{d}x}_{\text{Variation of expected number of particles}} = \\
&\quad = \underbrace{\int_t^{t+\mathrm{d}t} g(r,\tau)\, n(r,\tau)\ \mathrm{d}\tau - \int_t^{t+\mathrm{d}t} g(r+\mathrm{d}r,\tau)\, n(r+\mathrm{d}r,\tau)\ \mathrm{d}\tau\, +}_{\text{Difference in flux of growth entering and exiting the rectangle}} \\
&\quad\quad + \underbrace{\int_t^{t+\mathrm{d}t}\int_r^{r+\mathrm{d}r} k_n(x,\tau)\ \mathrm{d}x\ \mathrm{d}\tau}_{\text{Number of new nucleated particles}} - \underbrace{\int_t^{t+\mathrm{d}t}\int_r^{r+\mathrm{d}r} k_d(x,\tau)\, n(x,\tau)\ \mathrm{d}x\ \mathrm{d}\tau}_{\text{Number of disappearing particles}}\,. \qquad (40)
\end{aligned}$$

Dividing through by $\mathrm{d}r > 0$ and $\mathrm{d}t > 0$, and applying the limits $\mathrm{d}r,\ \mathrm{d}t \to 0$ we obtain the PBE

$$\frac{\partial n(r,t)}{\partial t} = -\frac{\partial\,(\,g(r,t)\,n(r,t)\,)}{\partial r} + k_n(r,t) - \,k_d(r,t)\,n(r,t), \quad \forall (r,t) \in [0,\infty)^2. \qquad (41)$$

The terms on the right hand side of (41) represent the mechanisms of transport, source and reaction. The transport term is driven by the particles growth, since the density $n(r,t)$ is shifted from left to right by the growth process. Nucleation provides the source term as the new nucleated particles act as a source of new particles. Finally, Ostwald ripening is represented by the reaction term, as it accounts for particle dissolution.

The boundary condition is specified as follows. Assuming that the particle growth flux is always zero, if evaluated at $r = 0$, for any choice of the growth function $g(r,t)$:

$$g(0,t)\,n(0,t) = 0, \quad \forall g,\ \forall t. \qquad (42)$$

If (42) does not hold, the particle radius r could adopt negative values as there would exist a non-zero flux pushing the particles towards negative radii values. This of course is not physically possible. Hence, (42) leads to the boundary condition:

$$n(0,t) = 0, \quad \forall t \in [0,\infty). \qquad (43)$$

Thus, given an initial distribution $\bar{n}(r)$, we propose the following PBE system to model the dynamics of the density $n(r,t)$:

$$\begin{cases}
\dfrac{\partial n(r,t)}{\partial t} = -\,\dfrac{\partial\,(\,g(r,t)\,n(r,t)\,)}{\partial r} + & \\
\qquad\qquad + k_n(r,t) - \,k_d(r,t)\,n(r,t) & \forall (r,t) \in [0,\infty)^2 \\
n(0,t) = 0 & \forall t \in [0,\infty) \\
n(r,0) = \bar{n}(r) & \forall r \in (0,\infty).
\end{cases} \qquad (44)$$

System (44) can be numerically integrated to predict the PSD behavior and to analyse the effects of the different processes driving the considered reaction.

5.2 A growth model

In this section we propose a simplified model. Vetter *et al.*, [21] highlighted the difficulties in modelling nucleation and growth simultaneously. One of the main issues is that the Ostwald ripening models require the particle critical radius to depend on supersaturation conditions, whereas nucleation models assume constant critical radius, i.e., $k_n(r,t)$ is a delta function. Moreover, the simplified growth model also fits with the experiments described in [4]. The initial condition, $\bar{n}(r)$, is interpreted as the PSD resulting from nucleation. Thus, nucleation and Ostwald ripening are neglected, and only growth processes are considered. We note that there is no restriction on the positiveness of the growth function. Thus, a negative growth function would lead to a decrease in particle size. PBE models only considering growth processes have been frequently used [22, 23]. Hence, ignoring nucleation and dissolution the reduced model is

$$\begin{cases} \dfrac{\partial n(r,t)}{\partial t} = -\dfrac{\partial\,(\,g(r,t)\,n(r,t)\,)}{\partial r} & \forall (r,t) \in [0,\infty)^2 \\ n(0,t) = 0 & \forall t \in [0,\infty) \\ n(r,0) = \bar{n}(r) & \forall r \in (0,\infty). \end{cases} \tag{45}$$

We use the growth function derived from Fick's first law, as given in [8]:

$$g(r,t) = \frac{V_M D(c_b(t) - s(r,t))}{r}\,, \tag{46}$$

where $c_b(t)$ is the bulk concentration, s the particle solubility, V_M the molar volume and D the diffusion coefficient. The particle solubility given by the modified OFC expression (34) accounts for the surfactant at the surface of the particles.

Assuming spherical particles, the total volume of particles is

$$V_p(t) = \frac{4\pi}{3}\int_0^\infty r^3\, n(r,t)\,\mathrm{d}r\,. \tag{47}$$

Hence, $m_s(t)$, the molar amount of surfactant is

$$m_s(t) = \frac{\rho_s}{M_s}\left[V_\theta(t) - V_p(t)\right]\,, \tag{48}$$

where ρ_s is the surfactant density, M_s is the surfactant molar mass and $V_\theta(t)$ is total volume of the particles including the constant surfactant layers with thickness θ in contact with each particle. Hence

$$V_\theta(t) = \frac{4\pi}{3}\int_0^\infty (r+\theta)^3\, n(r,t)\,\mathrm{d}r\,. \tag{49}$$

To complete the derivation of the model, we define the bulk monomer concentration $c_b(t)$ (similar to (24) in Section 3.3). Via mass conservation

$$c_b(t)M_pV_b(t) + \rho_pV_p(t) = c_b(0)M_pV_b(0) + \rho_pV_p(0)\,, \tag{50}$$

where $V_b(t)$ is the total volume of bulk. Upon rearranging 50 we obtain

$$c_b(t) = c_b(0)\frac{V_b(0)}{V_b(t)} + \frac{\rho_p}{M_p}\,\frac{V_p(0) - V_p(t)}{V_b(t)}\,. \tag{51}$$

Finally, the bulk total volume $V_b(t)$ is

$$V_b(t) = V_s - V_\theta(t)\,, \tag{52}$$

where V_s is the solution total volume, assumed to be constant.

Reduced model in the absence of citrate

A reduced version of the above model is when citrate is not present in the surrounding solution. The absence of citrate is equivalent to a surfactant layer with thickness $\theta = 0$. Hence, $V_\theta(t) \equiv V_p(t)$ for all t, and the molar fraction in (32) is always equal to one. Thus, assuming an ideal mixture, (i.e., $\gamma = 1$), the particle solubility reduces to

$$s(r,t) = s_\infty \exp\left({}^{\alpha}\!/_{r}\right), \tag{53}$$

which is the standard OFC. This particular choice of $\theta = 0$ allows us to analyse the model of Sugimoto in [8].

Zero order moment conservation

In this section, as defined by (45), we show that the number of particles is conserved throughout the process. In particular, in the absence of nucleation and dissolution, the total number of particles must be conserved, as the model only accounts for growth. The zero order moment $M^0(t)$ of the density function $n(r,t)$ corresponds to the expected total number of particles, and is defined to be

$$M^0(t) := \int_0^\infty n(r,t)\ \mathrm{d}r, \quad \forall t \in [0,\infty). \tag{54}$$

To verify particle number conservation, we need to show conservation of $M^0(t)$. We observe that

$$\frac{\mathrm{d}M^0(t)}{\mathrm{d}t} = \int_0^\infty \frac{\partial n(r,t)}{\partial t}\ \mathrm{d}r = -\int_0^\infty \frac{\partial\left(\, g(r,t)\, n(r,t)\,\right)}{\partial r}\ \mathrm{d}r = -\left[\, g(r,t)\, n(r,t)\,\right]_{r=0}^{r=\infty} = 0. \tag{55}$$

Consequently, $M^0(t)$ is a conserved quantity of system (45) and the total number of particles does not vary. We note that in (55) we exploit the zero growth flux as $r \to \infty$, i.e.,

$$\lim_{r\to\infty} g(r,t)n(r,t) = 0, \quad \forall g,\ \forall t\,, \tag{56}$$

analogous to (42).

5.3 Numerical integration scheme

Several numerical methods have been proposed to integrate PBE systems [24, 25, 26, 27, 28, 29]. In this section, we outline a numerical scheme to integrate the PBE system (45). As a first attempt, we used well-known fourth-order accurate techniques such as the composite Simpson's rule, central differences and Runge-Kutta methods. For the subsequent analysis, we refer to the dimensionless model outlined in Appendix B.1. The dimensionless tilde notation is neglected.

The first step of the numerical scheme involves the discretization of the equations in space. Given $h > 0$, we define the space discretization grid:

$$r_k := kh + r_{\min}, \quad \forall k = 0,..,N, \tag{57}$$

where $r_{\min} > 0$ is chosen such that $\forall r \in [0, r_{\min}]$ the density $n(r,t)$ is zero for $t \in [0,\infty)$. This assumption, which is in agreement with experimental results [4], also allows us to avoid any possible numerical singularities that may occur whilst evaluating the growth rate (46). Next, we define $n_k(t)$, as the value assumed by the density $n(r,t)$ for $r = r_k$,

$$n_k(t) := n(r,t)\big|_{r=r_k}\,, \quad \forall k = 0, .., N. \tag{58}$$

The boundary and initial conditions are:

$$n_k(0) = \bar{n}(r_k), \quad \forall k = 1, .., N, \tag{59}$$

$$n_0(t) = 0, \quad \forall t \in [0, \infty). \tag{60}$$

We note that imposing (60) is equivalent to setting $n_0(t) = n(r,t)\big|_{r=r_{\min}} = 0$.

The time derivative of $n_k(t)$ is given by, $\forall k = 1, .., N$:

$$\frac{\mathrm{d}n_k(t)}{\mathrm{d}t} = \left.\frac{\partial n(r,t)}{\partial t}\right|_{r=r_k} = -\left.\frac{\partial\,(\,g(r,t)\,n(r,t)\,)}{\partial r}\right|_{r=r_k} = -\zeta(r_k,t)\,n_k(t) - g(r_k,t)\,\left.\frac{\partial n(r,t)}{\partial r}\right|_{r=r_k}, \tag{61}$$

where $\zeta(r,t) := \partial g(r,t)/\partial r$. The details of its computation can be found in Appendix B.2. To complete the discretization in space, we approximate

$$\left.\frac{\partial n(r,t)}{\partial r}\right|_{r=r_k}, \quad \forall k = 1, .., N\,, \tag{62}$$

via the finite difference scheme

$$\left.\frac{\partial n(r,t)}{\partial r}\right|_{r=r_k} \approx \begin{cases} \frac{-n_{k+2}(t)+8n_{k+1}(t)-8n_{k-1}(t)+n_{k-2}(t)}{12h} & \forall k = 2, .., N-2 \\ \frac{25n_N(t)-48n_{N-1}(t)+36n_{N-2}(t)-16n_{N-3}(t)+3n_{N-4}(t)}{12h} & \text{if } k = N \\ \frac{3n_N(t)+10n_{N-1}(t)-18n_{N-2}(t)+6n_{N-3}(t)-n_{N-4}(t)}{12h} & \text{if } k = N-1 \\ \frac{n_4(t)-6n_3(t)+18n_2(t)-10n_1(t)-3n_0(t)}{12h} & \text{if } k = 1. \end{cases} \tag{63}$$

Extreme values of k, such as N, $N-1$ and 1, are not allowed in central difference schemes, because of the lack of either backward or forward grid points. This is why we propose non-central schemes for approximating the partial derivatives, thus allowing for k to take any value. Fourth-order accurate schemes are chosen for consistency with the accuracy of the numerical schemes proposed in the remaining part of this section. Specfically, the values assumed by the integral terms (47) and (49) must be approximated. Given (58), the candidate quadrature rules for computing (47) and (49) are based on interpolating functions, as the integrand functions are known only for a finite set of points. In particular, fourth-order accurate composite Simpson's rules are chosen to approximate the values of integral quantities $V_p(t)$ and $V_\theta(t)$:

$$V_p(t) = \int_0^\infty r^3\, n(r,t)\ \mathrm{d}r \approx \sum_{k=0}^{N} \omega_k\, r_k^3\, n_k(t), \quad \forall t \in [0, \infty), \tag{64}$$

$$V_\theta(t) = \int_0^\infty (r+\theta)^3\, n(r,t)\ \mathrm{d}r \approx \sum_{k=0}^{N} \omega_k\, (r_k+\theta)^3\, n_k(t), \quad \forall t \in [0, \infty), \tag{65}$$

$$\omega_k := \frac{i_k h}{3}, \quad i_k := \begin{cases} 1 & \text{if } k = 0, N \\ 4 & \text{if } k \equiv 1 \pmod 2 \,\wedge\, k \neq 0, N \\ 2 & \text{if } k \equiv 0 \pmod 2 \,\wedge\, k \neq 0, N, \end{cases} \quad \forall k = 0, .., N. \tag{66}$$

Composite Simpson's rules impose an even choice for the grid size N.

In summary, given the numerical approximations for the partial derivative (62) and the integral terms (47) and (49), the space discretization of the considered PBE system leads to the ODE system (61). A fourth-order accurate Runge-Kutta method in time is applied. The accuracy of the proposed method can be tested vis the conservation of the zero order moment from Section 5.2. It is shown in Appendix B.1 that

$$\int_0^\infty n(r,t)\ \mathrm{d}r = 1, \quad \forall t \in [0,\infty). \tag{67}$$

Consequently, one can propose the following test of accuracy of the solution via

$$\sum_{k=0}^{N} \omega_k\, n_k(t) \approx 1, \quad \forall t \in [0,\infty), \tag{68}$$

where ω_k is defined in (66).

5.4 Results

The results from the numerical scheme are presented in this section. The Mathlab solver *ode45* was used to generate the simulations. Two initial distributions were tested: (i) a unimodal Gaussian distribution and (ii) a bimodal Gaussian distribution for varying surfactant layer thicknesses, θ.

In Figure 1.10 we show the evolution of the distribution subject to the unimodal Gaussian initial condition for three different surfactant layer thicknesses: (a) $\theta = 0$, (b) $\theta = 1$ and (c) $\theta = 1.5$. In the absence of surfactant, i.e., $\theta = 0$, the PSD becomes broader with increasing time. However, when θ is increased to 1 or 1.5, size focussing is observed. The PSD becomes narrower with increasing time, whilst there is an increase in the mean particle radius.

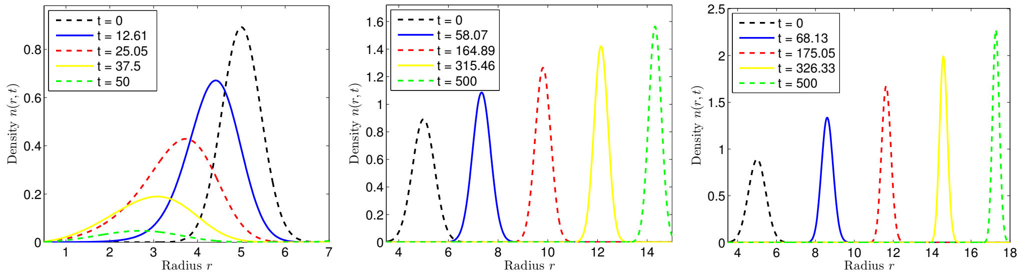

(a) $\theta = 0$ (b) $\theta = 1$ (c) $\theta = 1.5$

Figure 1.10: Evolution of PSD subject to initial unimodal Gaussian distribution for surfactant layers of different widths.

As discussed, the conservation of the zero moment $M^0(t)$ can be used to test the accuracy of the numerical scheme. In Figure 1.11 we show the conservation of $M^0(t)$ for the unimodal Gaussian initial condition. Conservation is only violated for $\theta = 0$, while for the other choices of θ, $M^0(t)$ is conserved. As shown in Figure 1.10(a), the reaction performed without surfactant, i.e., $\theta = 0$, reduces the size of the particles radius. This change in size makes the particles radius take on values smaller than $r_{\min}$ in (57). As a result, part of the density $n(r,t)$ disappears from the domain of integration $[r_{\min}, r_N]$. This is the cause of the violation of the $M^0(t)$ conservation. To avoid this issue, one can choose the value of $r_{\min} > 0$ to be as close as possible to zero. However, the model exhibits a singularity for $r = 0$ in (46). In other words, the value of $r_{\min} > 0$ cannot be set very close to zero. In any case, violating conservation of $M^0(t)$ is a well known issue in PBE approaches [30, 31].

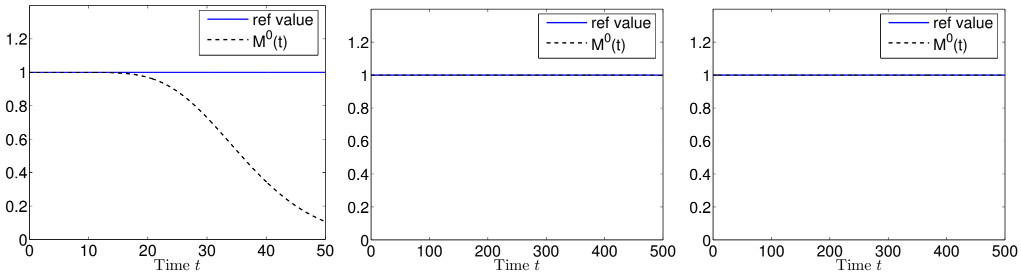

(a) $\theta = 0$ (b) $\theta = 1$ (c) $\theta = 1.5$

Figure 1.11: Zero order moment $M^0(t)$ conservation subject to initial unimodal Gaussian distriubtion. Conservation is violated when $\theta = 0$.

In Figure 1.12 we show the evolution of $n(r,t)$ subject to a bimodal Gaussian initial distributions for varying surfactant layer thicknesses. In this case, size focussing is observed when $\theta = 2$. When no surfactant is present the behavior is very similar to that which was observed in the unimodal Gaussian case. A layer of thickness $\theta = 0.5$ also proved to be too thin to observe size focusing. As in the unimodal case, we also show that the $M^0(t)$ conservation test in Figure 1.13. The results are consistent with those from the previous simulations, where θ sufficiently small leads to the conservation requirement.

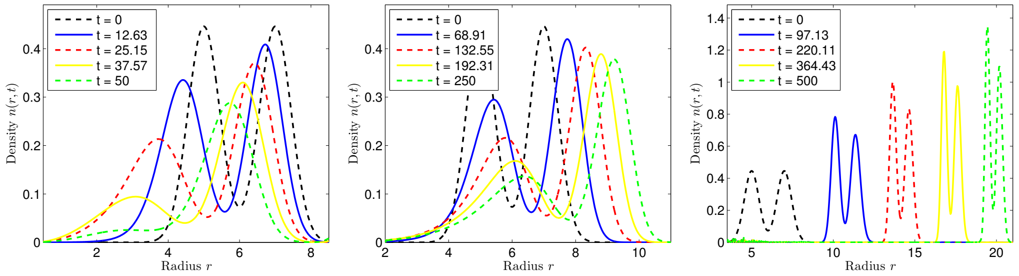

(a) $\theta = 0$ (b) $\theta = 0.5$ (c) $\theta = 2$

Figure 1.12: Evolution of PSD subject to initial bimodal Gaussian distribution.

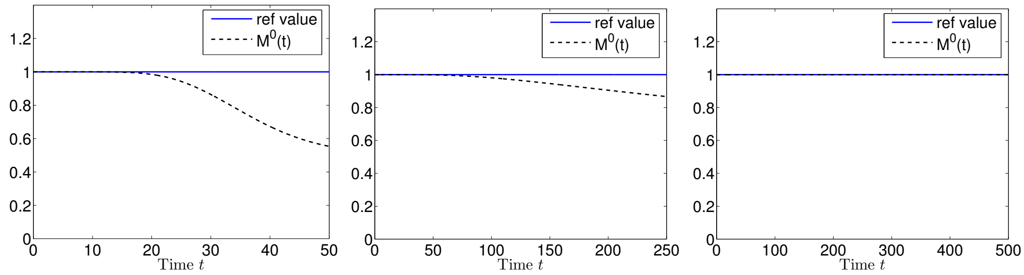

(a) $\theta = 0$ (b) $\theta = 0.5$ (c) $\theta = 2$

Figure 1.13: Zero order moment $M^0(t)$ conservation subject to initial bi-modal Gaussian distribution Conservation is violated for small values of θ.

5.5 Conclusions

The analysis of this section has shown the potential power of the PBE approach. The proposed PBE model shows the same qualitative behavior as that demonstrated in the experimental study of Bastús *et al.*, [4]. The current model formulation also allows for general settings and aims to deal with different phenomena that may occur during the crystallization processes. Although the current model was reduced to include only growth, a similar approach could be developed for the formulation in Section 5.1 to include nucleation and Ostwald ripening.

However, open questions remain. As observed in Section 5.4, the numerical scheme is not robust when the surfactant layer thickness θ becomes too small. The numerical integration is performed using the time independent distribution support $[r_{\min}, r_N]$ (see (57)). We suggest the usage of an interval adaptive in time to sharply bound the actual distribution support. Finer meshes could also be used whilst saving computational time by neglecting regions of no consequence, i.e., $n(r,t) \approx 0$. The choice of $r_{\min}$ can be also problematic, as discussed. On the one hand, it cannot be too close to zero, because it leads to a singularity in (46). However, it also cannot be an arbitrary choice, as being too far from zero would result in a loss of information due to a part of the reactant domain being excluded during the simulation. In addition, inaccurate initial conditions can lead to incorrect results.

Knowledge of the exact initial distribution of a population of particles would also significantly improve the numerical results. As we did not have access to the actual process parameters, we used parameters that we thought were of the correct order of magnitude (or approximately equal) to those in the IGN's synthesis process. One of our future tasks will be to obtain the correct parameter values, and hence obtain more accurate simulation results.

6 Summary and future work

The aim of this report was to use mathematical techniques to assist the ING in developing a better understanding of their nanoparticle from solution synthesis methods. Of particular interest was the relationship between the system parameters and the monodispersity of the final PSD. Three different approaches were applied.

In Section 3 we developed a differential equation model for the growth of a single particle and a system of N particles. We obtained good agreement between our numerical simulations and experimental data (from [7]) for CdSe particles. The model indicated that the addition of extra monomer improved the monodispersity of the PSD.

Next in Section 4, we proposed a possible mechanism to explain why Ostwald ripening is not observed in the ING's synthesis method. The main result was that the inclusion of citrate (as a stabilizer) in the solution leads to the formation of a monolayer on the nanoparticles. The introduction of this layer changes the particle solubility from a monotonic decreasing function of the particle radius (see Figure 1.5) to a function that can increase with particle size (see Figure 1.9). This change in solubility is the cause of Ostwald ripening inhibition.

Finally, in Section 5 a population balance equation approach was used to simulate the processes of size focussing and Ostwald ripening, and show their effect on the evolving PSD. The method captured the main qualitative features of the ING's synthesis methods.

We have identified possible extensions to the analysis which will be considered in subsequent studies. One of the critical future tasks is to validate our models with the results obtained by the ING. This will require us to obtain appropriate parameter values for the ING's synthesis methods. As highlighted, the ODE model of Section 3 showed good agreement with the data of Peng *et al.*, [7] so we are reasonably confident that the model can be used to describe the ING's data. We will then optimise the ING's synthesis method by varying the model parameters (e.g., temperature, monomer concentration). We will also seek strategies for monomer injection that enhance size focussing and inhibit Ostwald ripening.

6.1 Acknowledgements

V. Cregan, H. Ribera and M. Calvo were supported by "la Caixa" foundation grants. T. Myers, S. Serna, A. Marquina acknowledge the support of Ministerio de Ciencia e Innovación Grant MTM2014-56218.

Bibliography

[1] R.A. Freitas. Current status of nanomedicine and medical nanorobotics. *Journal of Computational and Theoretical Nanoscience*, 2(1):1–25, 2005.

[2] R.W. Siegel and E. Hu. *Nanostructure Science and Technology: R & D Status and Trends in Nanoparticles, Nanostructured Materials and Nanodevices.* Springer Science & Business Media, 1999.

[3] N.V. Mantzaris. Liquid-phase synthesis of nanoparticles: particle size distribution dynamics and control. *Chemical Engineering Science*, 60(17):4749–4770, 2005.

[4] N.G Bastús, J. Comenge, and V. Puntes. Kinetically controlled seeded growth synthesis of citrate-stabilized gold nanoparticles of up to 200 nm: size focusing versus Ostwald ripening. *Langmuir*, 27(17):11098–11105, 2011.

[5] N.G. Bastús, F. Merkoç, J. Piella, and V. Puntes. Synthesis of highly monodisperse citrate-stabilized silver nanoparticles of up to 200 nm: kinetic control and catalytic properties. *Chemistry of Materials*, 26(9):2836–2846, 2014.

[6] V.K. La Mer. Nucleation in phase transitions. *Industrial & Engineering Chemistry*, 44(6):1270–1277, 1952.

[7] X. Peng, J. Wickham, and A.P. Alivisatos. Kinetics of II-VI and III-V colloidal semiconductor nanocrystal growth: "focusing" of size distributions. *Journal of the American Chemical Society*, 120(21):5343–5344, 1998.

[8] T. Sugimoto. Preparation of monodispersed colloidal particles. *Advances in Colloid and Interface Science*, 28:65–108, 1987.

[9] R. Viswanatha and D.D. Sarma. Growth of nanocrystals in solution. *Nanomaterials Chemistry: Recent Developments and New Directions*, pages 139–170, 2007.

[10] D.V. Talapin, A.L. Rogach, M. Haase, and H. Weller. Evolution of an ensemble of nanoparticles in a colloidal solution: theoretical study. *The Journal of Physical Chemistry B*, 105(49):12278–12285, 2001.

[11] A. Baldan. Review progress in Ostwald ripening theories and their applications to nickel-base superalloys Part I: Ostwald ripening theories. *Journal of Materials Science*, 37(11):2171–2202, 2002.

[12] S.R. Coriell and R.L. Parker. Stability of the shape of a solid cylinder growing in a diffusion field. *Journal of Applied Physics*, 36(2):632–637, 2004.

[13] P.W. Voorhees. The theory of Ostwald ripening. *Journal of Statistical Physics*, 38(1-2):231–252, 1985.

[14] Z.A. Peng and X. Peng. Mechanisms of the shape evolution of CdSe nanocrystals. *Journal of the American Chemical Society*, 123(7):1389–1395, 2001.

[15] M.D. Clark, S.K. Kumar, J.S. Owen, and E.M. Chan. Focusing nanocrystal size distributions via production control. *Nano letters*, 11(5):1976–1980, 2011.

[16] V.M. Huxter, A. Lee, S.S. Lo, and G.D. Scholes. CdSe nanoparticle elasticity and surface energy. *Nano Letters*, 9(1):405–409, 2008.

[17] Isaac Ojea-Jiménez, Francisco M Romero, Neus G Bastús, and Victor Puntes. Small gold nanoparticles synthesized with sodium citrate and heavy water: insights into the reaction mechanism. *The Journal of Physical Chemistry C*, 114(4):1800–1804, 2010.

[18] G.W. Poehlein and L.A. Wenzel. *Theory of particulate processes-analysis and techniques of continuous crystallization.* Academic Press, 1972.

[19] S.E. LeBlanc and H.S. Fogler. Population balance modeling of the dissolution of polydisperse solids: rate limiting regimes. *AIChE Journal*, 33(1):54–63, 1987.

[20] D. Ramkrishna. *Population Balances: Theory and Applications to Particulate Systems in Engineering.* Academic Press, 2000.

[21] T. Vetter, M. Iggland, D.R. Ochsenbein, F.S. Hï¿½nseler, and M. Mazzotti. Modeling nucleation, growth, and ostwald ripening in crystallization processes: a comparison between population balance and kinetic rate equation. *Crystal Growth & Design*, 13(11):4890–4905, 2013.

[22] A. Mersmann. *Crystallization Technology Handbook.* CRC Press, 2001.

[23] J.W. Mullin. *Crystallization.* Butterworth-Heinemann, 2001.

[24] S. Kumar and D. Ramkrishna. On the solution of population balance equations by discretization - I. A fixed pivot technique. *Chemical Engineering Science*, 51(8):1311–1332, 1996.

[25] S. Kumar and D. Ramkrishna. On the solution of population balance equations by discretization - II. A moving pivot technique. *Chemical Engineering Science*, 51(8):1333–1342, 1996.

[26] S. Kumar and D. Ramkrishna. On the solution of population balance equations by discretization - III. Nucleation, growth and aggregation of particles. *Chemical Engineering Science*, 52(24):4659–4679, 1997.

[27] M. Nicmanis and M.J. Hounslow. Finite-element methods for steady-state population balance equations. *AIChE Journal*, 44(10):2258–2272, 1998.

[28] A.H. Alexopoulos, A.I. Roussos, and C. Kiparissides. Part I: Dynamic evolution of the particle size distribution in particulate processes undergoing combined particle growth and aggregation. *Chemical Engineering Science*, 59(24):5751–5769, 2004.

[29] D. Meimaroglou, A.I. Roussos, and C. Kiparissides. Part IV: Dynamic evolution of the particle size distribution in particulate processes. A comparative study between Monte Carlo and the generalized method of moments. *Chemical Engineering Science*, 61(17):5620–5635, 2006.

[30] R.C. Ball, C. Connaughton, T.H.M. Stein, and O. Zaboronski. Instantaneous gelation in smoluchowski's coagulation equation revisited. *Physical Review E*, 84(1):011111, 2011.

[31] R.C. Ball, C. Connaughton, P.P. Jones, R. Rajesh, and O. Zaboronski. Collective oscillations in irreversible coagulation driven by monomer inputs and large-cluster outputs. *Physical Review Letters*, 109(16):168304, 2012.

A A differential equation model for nanoparticle evolution

A.1 Numerical implementation

To solve the ODE system of N particles in Section 3.3 we used a finite difference numerical scheme. In particular, we discretise time with a time step Δt and approximate the time derivative in equation (25) using forward differences to give

$$\frac{r_{pi}^{n+1} - r_{pi}^{n}}{\Delta t} = \frac{c_b^n + \overline{s}_0 - s(r_{pi}^n)}{\overline{Da} + r_{pi}^n}, \tag{69}$$

where n denotes the n-th time step. We find the radius at the $(n+1)$-th time step via

$$r_{pi}^{n+1} = \Delta t \frac{c_b^n - \overline{s}_0 - s(r_i^n)}{\overline{Da} + r_{pi}^n} + r_{pi}^n. \tag{70}$$

To study the evolution of the particle population there are two key parameters, namely the mean radius and standard deviation at each time step. These are given by

$$\bar{r}^n = \frac{1}{N^n}\sum_{i=1}^{N} r_{pi}^n\,, \quad \sigma^n = \left(\frac{1}{N^n-1}\sum_{i=1}^{N}\left(\bar{r}^n - r_{pi}^n\right)^2\right)^{1/2}\,, \tag{71}$$

respectively, where N^n is the number of nanoparticles in the system at the n-th time step. The pseudocode used to generate the results is outlined below.

Listing 1: `r` denotes the radii distribution at each time step, `N_NP` denotes the number of nanoparticles in the system, `mean_id` and `sd_id` the mean and standard deviation of the initial particle distribution respectively, `cb` denotes the monomer concentration in solution, `s` the particle solubility, `s_infty` the bulk particle solubility, `s_0` is $s_{\bar{r}_0}$, and `Dc` is Δc.

```
% obtain the vector of initial radii
r(1:N_NP) = sd_id*randn(1,N_NP) + mean_sd;

% in case some of the radius is negative we make it positive
for i = 1:N_NP
        while r(i) <= 0
                r(i) = sd_id*randn(1,1) + mean_sd;
        end
end

for n = 2:t_steps
        s(n,:) = (s_infty*exp(alpha/r))-s_0)/Dc;
        ind_nonzero = find(r~=0);
        r(ind_nonzero) = dt*(Cb(n-1)-s(n,ind_nonzero))/r(ind_nonzero)
                       + r(ind_nonzero);
    r(r<=0) = 0;

        cb(n) = % see equation (9);

        mean_r(n) = % see equation (11);
        sd(n) = % see equation (11);
end
```

B Population balance equation approach

B.1 Dimensionless growth model

In this appendix a dimensionless version of the growth model in Section 5.2 is proposed. We begin by introducing the dimensionless variables:

$$\tilde{r} := \frac{r}{\alpha}, \quad \tilde{t} := \frac{t}{\tau}, \quad \tilde{n}(\tilde{r},\tilde{t}) := \frac{n(r,t)}{\nu}, \tag{72}$$

where α is the capillarity length, τ is a characteristic process time scale and ν is a characteristic value of the density $n(r,t)$. The value of α is a known experimental parameter, whilst the scaling factors τ and ν are to be determined.

The scaling factor ν is chosen to ensure computationally tractable orders of magnitude for the zero order moments of the dimensionless density $\tilde{n}(\tilde{r},\tilde{t})$. In Section 5.2 it was shown that the zero order moment of density $n(r,t)$ is a conserved quantity of system (45). The scaling (72) retains the conservation of the zero order moment. Thus, the dimensionless zero order moment of density $\tilde{n}(\tilde{r},\tilde{t})$ is a constant value. One can impose a constant value via

$$\int_0^\infty \tilde{n}(\tilde{r},\tilde{t})\ \mathrm{d}\tilde{r} = \int_0^\infty \tilde{\bar{n}}(\tilde{r})\ \mathrm{d}\tilde{r} = 1, \quad \forall \tilde{t} \in [0,\infty), \tag{73}$$

where $\tilde{\bar{n}}(\tilde{r}) := \bar{n}(r)/\nu$, and $\bar{n}(r)$ the initial condition of PBE system (45), which has a strictly positive zero order moment. Expression (73) can then be rewritten as

$$\frac{1}{\alpha\,\nu}\int_0^\infty \bar{n}(r)\ \mathrm{d}r = 1, \tag{74}$$

which yields a definition for the scaling factor ν:

$$\nu := \frac{1}{\alpha}\int_0^\infty \bar{n}(r)\ \mathrm{d}r > 0\,. \tag{75}$$

Considering the relations in (72), the total volume of the particles $V_p(t)$ can be rewritten as

$$V_p(t) = \left(\frac{4\pi}{3}\alpha^4\nu\right)\int_0^\infty \tilde{r}^3\,\tilde{n}(\tilde{r},\tilde{t})\ \mathrm{d}\tilde{r}. \tag{76}$$

Thus, we define its dimensionless counterpart to be

$$\tilde{V}_p(\tilde{t}) := \frac{V_p(t)}{\left(\frac{4\pi}{3}\alpha^4\nu\right)} = \int_0^\infty \tilde{r}^3\,\tilde{n}(\tilde{r},\tilde{t})\ \mathrm{d}\tilde{r}. \tag{77}$$

Given $\tilde{\theta} := \theta/\alpha$, we propose the equivalent scaling for the volume $V_\theta(t)$:

$$V_\theta(t) = \left(\frac{4\pi}{3}\alpha^4\nu\right)\int_0^\infty (\tilde{r}+\tilde{\theta})^3\,\tilde{n}(\tilde{r},\tilde{t})\ \mathrm{d}\tilde{r} \quad \Longrightarrow \quad \tilde{V}_\theta(\tilde{t}) := \frac{V_\theta(t)}{\left(\frac{4\pi}{3}\alpha^4\nu\right)} = \int_0^\infty (\tilde{r}+\tilde{\theta})^3\,\tilde{n}(\tilde{r},\tilde{t})\ \mathrm{d}\tilde{r}. \tag{78}$$

Once all the scaling factors above are known, we have:

$$m_p(t) = \left(\frac{4\pi}{3}\frac{\rho_p}{M_p}\alpha^4\nu\right)\tilde{V}_p(\tilde{t}) \quad \Longrightarrow \quad \tilde{m}_p(\tilde{t}) := \frac{m_p(t)}{\left(\frac{4\pi}{3}\frac{\rho_p}{M_p}\alpha^4\nu\right)} = \tilde{V}_p(\tilde{t}), \tag{79}$$

$$m_s(t) = \left(\frac{4\pi}{3}\frac{\rho_s}{M_s}\alpha^4\nu\right)\left[\tilde{V}_\theta(\tilde{t}) - \tilde{V}_p(\tilde{t})\right] \quad \Longrightarrow \quad \tilde{m}_s(\tilde{t}) := \frac{m_s(t)}{\left(\frac{4\pi}{3}\frac{\rho_s}{M_s}\alpha^4\nu\right)} = \tilde{V}_\theta(\tilde{t}) - \tilde{V}_p(\tilde{t}), \tag{80}$$

$$x_p(t) = \frac{\frac{\rho_p}{M_p}\tilde{m}_p(\tilde{t})}{\frac{\rho_p}{M_p}\tilde{m}_p(\tilde{t}) + \frac{\rho_s}{M_s}\tilde{m}_s(\tilde{t})} \quad \Longrightarrow \quad \tilde{x}_p(\tilde{t}) := x_p(t) = \frac{\tilde{m}_p(\tilde{t})}{\tilde{m}_p(\tilde{t}) + \beta\tilde{m}_s(\tilde{t})}, \quad \beta := \frac{\rho_s M_p}{\rho_p M_s}, \tag{81}$$

$$V_b(t) = \left(\frac{4\pi}{3}\alpha^4\nu\right)\left[v_s - \tilde{V}_\theta(\tilde{t})\right], \quad v_s := \frac{V_s}{\left(\frac{4\pi}{3}\alpha^4\nu\right)} \quad \Longrightarrow \quad \tilde{V}_b(\tilde{t}) := \frac{V_b(t)}{\left(\frac{4\pi}{3}\alpha^4\nu\right)} = v_s - \tilde{V}_\theta(\tilde{t}), \tag{82}$$

$$c_e(r,t) = s_\infty \gamma \tilde{x}_p(\tilde{t}) \exp\left({}^1\!/_{\tilde{r}}\right) \quad \Longrightarrow \quad \tilde{c}_e(\tilde{r},\tilde{t}) := \frac{c_e(r,t)}{s_\infty} = \gamma \tilde{x}_p(\tilde{t}) \exp\left({}^1\!/_{\tilde{r}}\right). \tag{83}$$

Then, the concentration $c_b(t)$ can be rewritten as:

$$c_b(t) = c_b(0)\frac{\tilde{V}_b(0)}{\tilde{V}_b(\tilde{t})} + \frac{\rho_p}{M_p}\frac{\tilde{V}_p(0) - \tilde{V}_p(\tilde{t})}{\tilde{V}_b(\tilde{t})}. \tag{84}$$

Hence, we can scale $c_b(t)$ with $c_{\max} := \max\{c_b(0), {}^{\rho_p}\!/_{M_p}\}$. We then define the dimensionless concentration to be

$$\tilde{c}_b(\tilde{t}) := \frac{c_b(t)}{c_{\max}} = \lambda_1\frac{\tilde{V}_b(0)}{\tilde{V}_b(\tilde{t})} + \lambda_2\frac{\tilde{V}_p(0) - \tilde{V}_p(\tilde{t})}{\tilde{V}_b(\tilde{t})}, \quad \lambda_1 := \frac{c_b(0)}{c_{\max}} \leq 1, \quad \lambda_2 := \frac{\rho_p}{c_{\max}M_p} \leq 1. \tag{85}$$

Thus, the growth rate $g(r,t)$ can be rewritten as

$$g(r,t) = \left(\frac{V_M\, D}{\alpha}\right)\frac{c_{\max}\tilde{c}_b(\tilde{t}) - s_\infty \tilde{c}_e(\tilde{r},\tilde{t})}{\tilde{r}}. \tag{86}$$

Proceeding as above, we define the maximum $g_{\max} := \max\{c_{\max}, s_\infty\}$ and the dimensionless growth rate to be

$$\tilde{g}(\tilde{r},\tilde{t}) := \frac{g(r,t)}{V_M\, D\, \alpha^{-1}\, g_{\max}} = \frac{\lambda_3\tilde{c}_b(\tilde{t}) - \lambda_4\tilde{c}_e(\tilde{r},\tilde{t})}{\tilde{r}}, \quad \lambda_3 := \frac{c_{\max}}{g_{\max}} \leq 1, \quad \lambda_4 := \frac{s_\infty}{g_{\max}} \leq 1. \tag{87}$$

In conclusion, the PBE (45) rewritten in dimensionless form is

$$\frac{\partial \tilde{n}(\tilde{r},\tilde{t})}{\partial \tilde{t}} = -\lambda_g \frac{\partial\left(\tilde{g}(\tilde{r},\tilde{t})\, \tilde{n}(\tilde{r},\tilde{t})\right)}{\partial \tilde{r}}, \quad \lambda_g := \frac{V_M\, D\, g_{\max}\, \tau}{\alpha^2}. \tag{88}$$

By imposing the factor λ_g equal to 1, we obtain the time scale

$$\tau := \frac{\alpha^2}{V_M\, D\, g_{\max}}\,. \tag{89}$$

B.2 Computation of the growth function derivative

In this appendix we compute the function $\zeta(r,t)$ as the partial derivative of $g(r,t)$ with respect to the particles radius r. Using the dimensionless definition of g in (87) we obtain

$$\zeta(r,t) = \frac{\partial g(r,t)}{\partial r} = -\lambda_3\frac{c_b(t)}{r^2} - \lambda_4\left[\frac{\frac{\partial c_e(r,t)}{\partial r}r - c_e(r,t)}{r^2}\right]. \tag{90}$$

The derivative of the concentration c_e in (83) is

$$\frac{\partial c_e(r,t)}{\partial r} = -\gamma x_p(t) \exp\left(\frac{1}{r}\right)\frac{1}{r^2}. \tag{91}$$

and thus,

$$\zeta(r,t) = -\lambda_3 \frac{c_b(t)}{r^2} + \lambda_4 \frac{\gamma x_p(t) \exp\left(\frac{1}{r}\right)\frac{1}{r} + c_e(r,t)}{r^2} = -\lambda_3 \frac{c_b(t)}{r^2} + \lambda_4 c_e(r,t)\frac{1+r}{r^3}. \tag{92}$$

Searching for a Predictive Model for Burglaries in Catalonia

Problem presented by
Pere Boqué[1]

Report prepared by
Maria Aguareles[2,9], Dusan Bikov[3], Marta Canadell[4], Enric Costa-Miracle[5], Carlos Domingo[6], Jesús Fernández-Sánchez[7], Núria Folguera[5], Jordi Saludes[7], Aleksandra Stojanova[3], Zlatko Varbanov[8]

Study group contributors
Maria Aguareles[2,9], Dusan Bikov[3], Marta Canadell[4], Enric Costa-Miracle[5], Carlos Domingo[6], Jesús Fernández-Sánchez[7], Núria Folguera[5], Jordi Saludes[7], Isabel Serra[5], Aleksandra Stojanova[3], Zlatko Varbanov[8]

Abstract: In this report we present a summary of the discussions and results obtained during the 115th European Study Group with Industry on the prediction of burglaries in Catalonia. This problem was presented by the Police Department and the goal was to obtain models for the dynamics of burglaries and to infer spatial and temporal patterns based on data from 2010 until 2015.

1 Statement of the problem

Mossos d'Esquadra is the name of the Police Department in Catalonia who have competences for prevention and investigation of criminal actions concerning civil security. In the last years burglaries have been one of the most relevant offences that they have dealt with. These are serious offences against citizens privacy which, in many occasions, end up with

---

[1] Mossos d'Esquadra de Catalunya, Sabadell, Spain
[2] Universitat de Girona, Girona, Spain
[3] Goce Delcev University, Stip, Macedonia
[4] Brown University, USA
[5] Centre de Recerca Matemàtica, Barcelona, Spain
[6] Universitat de Barcelona, Barcelona, Spain
[7] Universitat Politècnica de Catalunya, Barcelona, Spain
[8] University of Veliko Turnovo, Bulgary
[9] Report co-ordinator: maria.aguareles@udg.edu

intimidation and violence. Furthermore, these type of crimes take place all around the catalan territory and in all sort of environments, they occur in both flats and houses and at any time of the year. Recently, the Mossos d'Esquadra have been especially interested in the possibility of preventing burglaries by using prediction models.

Some cities around the world (see for instance [6]) have already implemented civil security strategies based on mathematical predicting tools. However, these tools strongly rely on a certain degree of regularity in the city planning and in the fact that offenders tend to choose their next target mainly according to a geographical proximity. This is, in fact, the major drawback when one tries to implement these models in Catalonia, where the territory is very heterogeneous. Cities in Catalonia combine very different types of homes, and it is very common to find neighbourhoods with detached houses and dense sets of flat buildings. Also, the structure and urbanisation of large cities and small towns is very different. According to police experience, burglars tend to specialize in particular types of households and so they move according to parameters which go beyond the physical proximity of houses. For instance, burglars often choose to burglarize places with fast escaping routes which are close to highways, or houses with particular types of fences or doors, etc.

In this report we present the results of the analysis of burglary data provided by *Mossos d'Esquadra* and we propose different approaches to derive predicting models, thus improving the algorithms that the police are now using. We start by exploring if geographical proximity patterns (the so-called *near-repeat victimisation*) can be deduced from the data. We then first consider small regions, of the level of small cities, to devise if waves of burglaries take place in concentrated periods of time. We thus remove the spatial dependence of the data in this first approach. As we shall show, several features arise from this first analysis: first, we observe that patterns arise only if a certain level of layer information is used, and secondly we observe that if one considers small towns or cities, it is indeed possible to predict the lapse of time between two consecutive waves of burglaries in the town. We then broaden our analysis to the possibility of having non-trivial spatial patterns of criminal activity. In particular we propose an algorithm to derive connections between different regions of Catalonia, that is to say, the goal is to detect if two given sets of burglaries which have taken place in regions that may be far away from each other have any relation at all, in the sense that when a burglary takes place in, for instance, region A, it is highly probable that burglaries in B will also take place. Finally we propose a model

2 Results

2.1 Exploring repeat-victimisation

The algorithms presented by the Mossos d'Esquadra in their initial exposition were based on the theory of repeat (or near-repeat) victimization. This criminology theory states that it is expectable that a target (in our case, a household or an area) suffers from repeated criminal victimization in a short period of time. *Near repeats* refer to targets with similar characteristics or situations, in the sense that the metric of the model is not necessarily determined only by spatial distance. This idea can be modeled by means of the so-called Hawkes process. The Hawkes process is a self-exciting point process that was introduced in seismology to model earthquakes and their aftershocks. More precisely, one assumes that there is a background rate at which events are likely to occur, and once an event does occur, the rate jumps up and aftershocks are expected to follow. See [2] for an application of this theory to gang rivalries in Los Angeles. The original algorithm that the Mossos d'Esquadra presented divided the territory in rectangular cells. Then, using data from the previous two weeks, they determined the potential risk of burglary in each cell for the following days. The algorithm heavily relied on the assumption that there was a near-repeat victimization phenomenon. However, the consideration of uncategorized events can hide these patterns. For instance, if we represent the burglaries in Sant Feliu de Guíxols[2] over time, it is hard to see any temporal cluster supporting the idea of repeated victimization (see Figure 1).

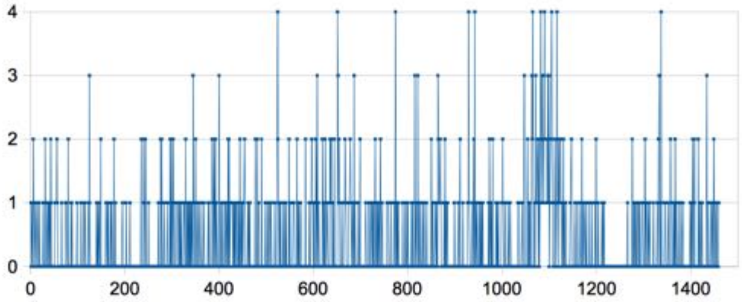

Figure 1: Total number of burglaries in Sant Feliu de Guíxols. 2011–14.

Given the information that we had at hand about each burglary (mainly, the type of construction), we decided to plot the same diagram but only for events that took place in country houses (see Figure 2). In this case, one can observe that there are temporal clusters that may be explained by a near-repeat victimization model, even in the case of Girona[3] city (see Figure 3).

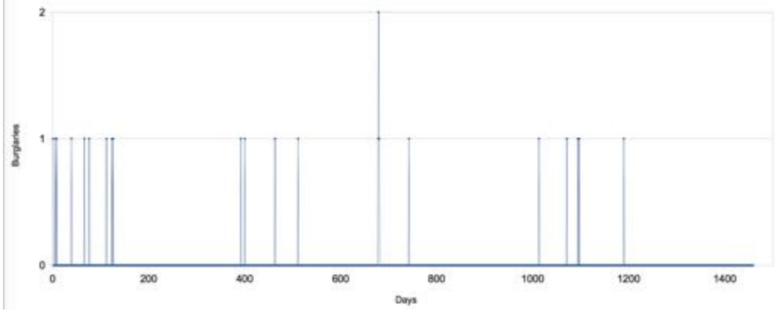

Figure 2: Burglaries in Country Houses in Sant Feliu de Guíxols. 2011–14.

Sticking to the same category of country houses, we also plotted the burglaries in the whole region of Girona[4]. In this case, the presence of temporal clusters is not as obvious (see Figure 4), so even if we are considering a particular type of burglary, the size of the region is still important if we want to find repetition patterns.

---

[2] 16,23 km^2 and 21.810 inhabitants.

[3] 39,14 km^2 and 97.227 inhabitants

[4] 5.905 km^2 and 756.810 inhabitants.

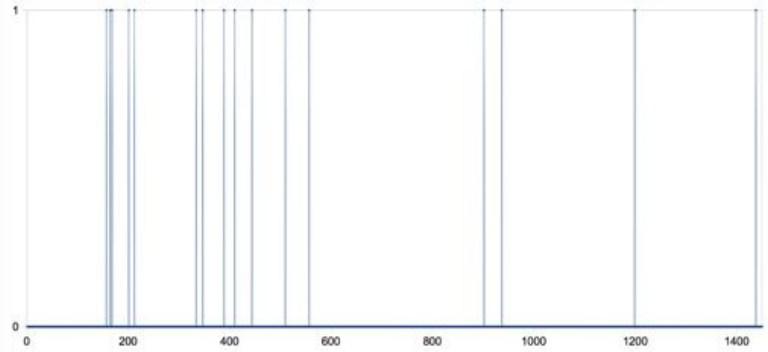

Figure 3: Burglaries in Country Houses in Girona City. 2011–14.

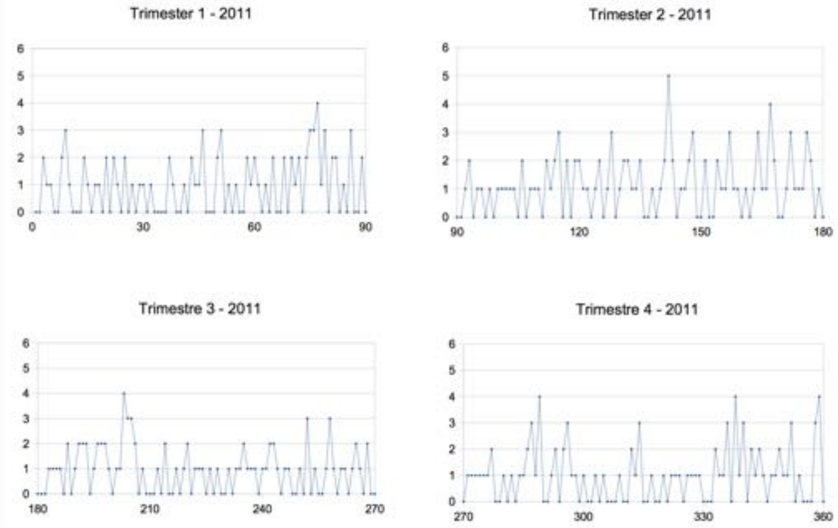

Figure 4: Burglaries in Country Houses in the Girona region. 2011 in trimesters.

A similar test can be carried out with other types of households (apartments, or houses), but these categories seem to be too broad (see Figure 5).

However, we are confident that if we could add additional data such as loot type in order to create subcategories, there is a chance that we could observe patters as in the country houses of Sant Feliu de Guíxols. Summing up, it could be useful to

- Define spatial cells adapted to the territory, using qualitative information such as the orography or demography of the area.
- Categorize burglaries in a few classes that can help us classify different kinds of events.
- Define different layers in each cell consisting of households (or areas) that could be potential targets of each class of burglary.

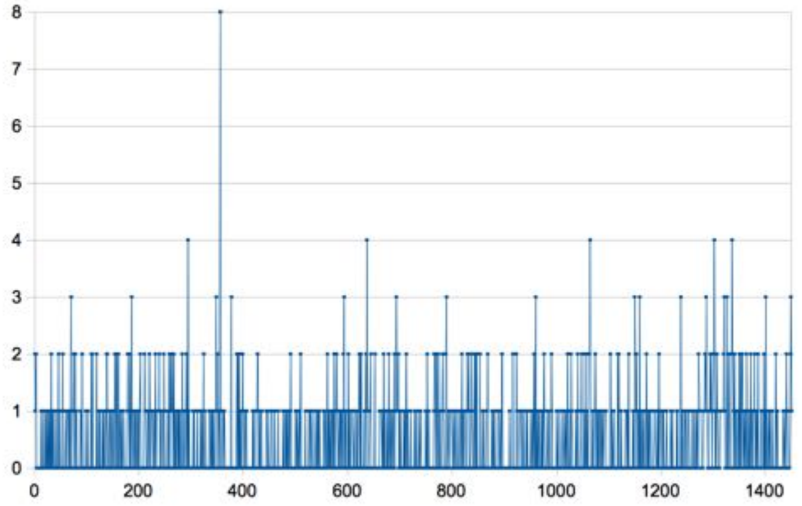

Figure 5: Burglaries in Apartments in Girona City. 2011–14.

- Run a near-repeat victimization based algorithm on each layer of each cell independently, using just the data of the corresponding class.

2.2 Time-dependent statistical analysis

To efficiently manage police resources, the Mossos d'Esquadra need some information of when and where the next wave of burglaries is most likely to take place. As a first approximation we have clustered the information at the level of cities and towns and we have computed the elapsed time between consecutive waves of events. The goal is to devise for each town whether there is a mean for this waiting time between events, which would indicate how long after a wave of burglaries in a city or town a new wave is expected.

We have used data corresponding to years from 2010 to 2014 and we have analysed it by means of the coefficient of variation, CV. The coefficient of variation, CV, is a standardized measure of dispersion of a probability distribution, that is to say, it explains the extent of variability in relation to the mean of the data studied. More precisely, it is defined as

$$CV = \frac{\sigma}{\mu}, \tag{1}$$

where σ is the standard deviation and μ is the mean of the sample.

In general, when studying this ratio, three main cases must be distinguished depending on how far from unity this quantity is:

- $CV \ll 1$ implies that the variance is very small with respect to the mean and therefore the events take place in almost a periodic way. For instance, this could imply that a burglaries are occurring every two days or once per week (the same day of the week). In this case, the corresponding density function is a Dirac delta and there clearly is a time pattern in the burglaries.
- $CV \simeq 1$ implies that the mean and the standard deviation are of the same order. In this case, when the standard deviation of an exponential function is equal to

its mean, the waiting time distribution function decays like an exponential. Exponential density functions correspond to Poisson processes which have been used to model near-repeat victimisation models (see for instance [3]). This models assume that if there is an offence in a given area, the probability that the burglars may strike in the same place or nearby is higher than in other places. This high probability prevails for a short time and it rapidly falls afterwards.

- When $CV \gg 1$ the data has a high-variance with respect to the mean. In this case, the distribution function for the waiting times does not decay exponentially but it has a fat tail. This is due to the presence of cluster formations in time since the events are self-attracting or self-activating. This would correspond to an scenario where the waves of burglaries last longer than just one day and they are followed by a longer period of peace.

We then want to compute the values for the coefficient of variation for some cities and towns in Catalonia. We first start by removing the zero waiting time events from the data, or, in other words, we don't take into account if a given day one or more events have taken place. The coefficient of variation after having removed the 0-waiting time events is usually known as the coefficient of variation of the residuals (CVR).

When computing the CVR for all the cities/town/villages available in the data, we observe the three different regimes explained above. For instance, the city of Sabadell, which is a medium size city, is found to have a CVR well bellow one. Amposta, which is a smaller town, has $CVR \simeq 1$ and El Bruc, that is even smaller, has $CVR >> 1$. In general we observe that large cities tend to have $CVR \ll 1$ but its mean is 1 day, which simply says that there are burglaries every day. This, in fact, does not give any information in terms of prevention and it is clear that it is due to the high population density in these cities. It is clear that in these cases one must consider smaller areas, probably at the level of neighbourhoods. At the other end, very small towns seem to have CVR well over one. It makes sense that in these towns or villages clusters appear since these locations are not so well-connected by public transport or main roads. Then, once the burglars move there, they stay around for a period of time. In table 1 we show the names of the cities in Catalonia where the CVR has been found to be greater than 1 and the ones where it has been found to be bellow 1:

$CVR \ll 1$	$CVR \ll 1$	$CVR \gg 1$
Barcelona	Sabadell	Begur
Tarragona	Reus	Cabrils
Girona	Santa Coloma de Gramenet	Creixell
Lleida	Mataró	El Bruc
Terrassa	Badalona	Sant Hilari Sacalm

Table 1: Cities with a $CVR \ll 1$ (1st and 2nd colum) and with $CVR \gg 1$ (3rd column).

Having a quick look at the table and knowing a little bit about Catalonia, the first feature that can be deduced is that large cities like Barcelona tend to have a very defined mean ($CVR \ll 1$), but, as in the case of Barcelona in all these cities the mean is of one day. In order to check this feeling in a more analytical way, we decided to search at the Catalan Institute of Statistics (Idescat) the number of inhabitants of these cities. In Table 2, we can see the number of inhabitants of the 11th largest cities in Catalonia:

An approach that the Mossos d'Esquadra were using was, in fact, to divide the whole Catalonia in cells and to investigate the evolution of events in each of these cells according to a near-repeat victimisation approach. In their simulations they already noticed that a crucial point is the size of such cells. In this sense, they were interested in understanding the optimal size of a cell in terms of predictions. Our conclusion with this results is that the same cell size cannot be used in all Catalonia and large cities require a more local analysis. As an example we have also computed the CVR for each neighbourhood in Barcelona and, in this case the CVR becomes of order one, thus implying that a near-repeat victimisation might be taking place. There are also other cities, like Granollers, where Mossos d'Esquadra had explicitly checked that near-repeat victimisation models where giving good predictions. Our conjecture is that only in areas where the CVR is close to one such near-victimisation models will be useful. In this sense, the CVR may be used as a tool to decide which cities require a more local analysis.

Position in the ranking	City	Number of inhab.
1	Barcelona	1.604.555
2	L'Hospitalet de Llobregat	252.171
3	Badalona	215.654
4	Terrassa	215.214
5	Sabadell	207.814
6	Lleida	138.542
7	Tarragona	131.255
8	Mataró	124.867
9	Santa Coloma de Gramenet	116.950
10	Reus	103.194
11	Girona	97.586

Table 2: Largest cities in Catalonia, IDESCAT, 2015.

To sum up we can conclude several things. The first one is that there seems to be a clear relationship between the number of inhabitants of the place we are studying and the value of the CVR. Large cities have $CVR << 1$ and thus, the near and repeat victimization pattern cannot be applied straightforward since it will not work. A new methodology should be designed and it seems that splitting the city into neighbourhoods and then applying the cells' model could be useful.

For medium size cities, that is cities that have between 10000 and 100000 inhabitants, which normally have $CVR \simeq 1$, near-repeat victimization models should suit well as it happened with Granollers. For the towns and villages, usually with $CVR >> 1$, we know that there are going to be clusters but we cannot assume that a near-repeat victimisation model will work. In this cases there might be connections with cells which are which are easily reached through highways, for instance. This idea will be more detailed in the following section.

2.3 Exploring spatio-temporal patterns

Repeat victimisation does not only occur in the shape of hot-spot. That is to say, there might be burglars who prefer to operate in the vicinity of highways and so they strike in places that are kilometres apart from each other. We want to infer these type of relations by exploring the data. To this aim, we have tried to design a model as simple as possible that allows to predict burglaries in terms of the data provided by the mossos. We propose the following algorithm:

- Start by partitioning the region in N cells (the smaller, the most accurate).
- We now define $f(i,j,\ell)$ as the ”influence" of cell j on cell i during a time span of ℓ (for instance, ℓ could be 1 or 2 weeks):

$$f(i,j;\ell) := \text{number of events in cell } j \text{ occurring in a period of} \\ \ell \text{ time steps after an event occurs in } i$$

- A contingency table (or matrix) $F(\ell)$ is constructed in this way for each value of ℓ. The bigger the entries the more related the cells i and j are.
- By normalizing the rows of this matrix so that each sums to one, we obtain a transition matrix $P(\ell)$, whose entries are estimates of the conditional probablilities

$$p(i|j;\ell) = \text{probability of an event in cell } j \text{ after an event } i \text{ in a} \\ \text{time window of length } \ell.$$

- After a burglary event occurs in one cell, say i, the maxima among the entries of the corresponding row i of $P(\ell)$ should indicate the cells where it is more probable that another burglar event occurs in the following ℓ weeks. Moreover, studying the monotony of the sequence $\{p(i|j;\ell)\}_\ell$ we can measure how long is the influence of cell j in cell i.

Remark 1. A similar analysis can be performed restricting data to events recorded after some particular date k_0. The corresponding tables $F(\ell;k_0)$ and $P(\ell,k_0)$ should allow conclusions about the influence between cells in terms of the seasons or periods of the year. For example, different weeks of the year (different dates k_0) may produce different influence between cells. Parameters k_0 and ℓ allow different analysis and would play an important role for the analysis.

Remark 2. One could apply statistical analysis (namely, compute the chi-square statistic) to test if the data contained in the table $F(\ell)$ reveal dependence or independence between the events registered. Another approach would be to estimate how far the contingency table is from having rank one (this meaning independence among variables). To this aim, one can compute the singular values $\{\sigma_m\}_m$ of the matrix $F(\ell)$ and estimate the distance of $F(\ell)$ to the space of matrices of rank 1 as $\sqrt{\sum_{m\geq 2}\sigma_m^2}$. This kind of analysis should allow to validate or reject the near-repeat victimization assumption between cells or in a specified group of cells (for example, cells in the area of Barcelona).

This procedure should be improved by considering data associated to 1st or 2nd residence, or data of the metropolitan area and data of less-populated territories separately. As stated before, some amount of layer information might be helpful to detect patterns.

2.4 Graph theory

In this section we describe a method to simulate street networks in a city and to use them to detect possible hotspots. The idea is to think of the network map as a graph. The classical way to model the street network map is: the vertices of the graph represent the intersections between the streets and the links represent the streets which connect the intersections. A positive integer number (called *weight*) can be assigned to any link. In classical models the weight is the physical length of the street but for the purpose of this work this weight can be defined as a value of a function with more arguments: the physical length, the density of the flats/houses, the number of people living there, etc.

We shall denote by $G = (V, E)$ a graph (network) where $V = \{v_1, \ldots, v_n\}$ is a non-empty set of n vertices (nodes) and $E \subseteq V \times V$ is a set of links (edges) which connect them. In figure 6 we show an example of a network represented by a graph.

Finding hot spots One method to find possible hot spots for crimes (especially burglaries) was presented by T. Davies and S. Bishop (2013). A *path* in a network is defined as an ordered sequence of vertices such that there exists a link between any two consecutive vertices. The *length* of the path is the number of links (for an undirected graph) or the sum of weights of these links (for a directed graph). The *shortest path* between two vertices i and j (if there exists paths between them) is the one with minimal length. The so called *Betweenness centrality* is a measure which quantifies how often individual links are used during journeys through the network. These are the main steps to calculate this measure:

1. initialize all links with a betweennes centrality of 0;
2. consider all pairs of nodes i and j;
3. for each pair i and j, find the shortest path(s) between them;
4. for every link that appears in the shortest path(s), increment its betweenness centrality by $1/w$, where w is the number of shortest paths between i and j

More formally, if σ_{ij} is the total number of shortest paths between i and j, and $\sigma_{ij}(e)$ is the total number of shortest paths between i and j which contain the link $e \in E$, the betweenness centrality $C^b(e)$ of a given link can be defined as:

$$C^b(e) = \sum \frac{\sigma_{ij}(e)}{\sigma_{ij}}$$

for all vertices i, j such that there exists a path between i and j.

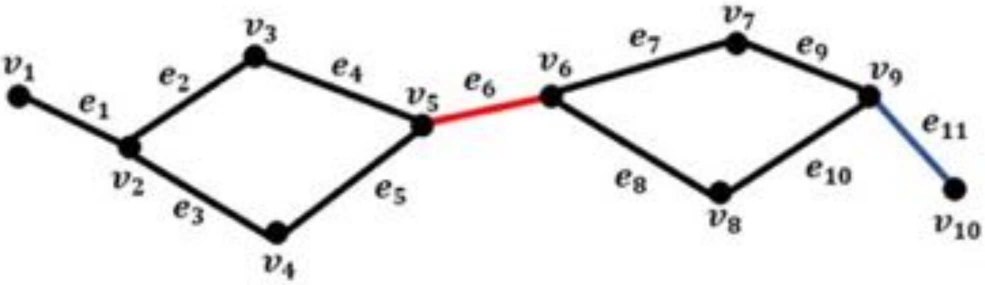

Figure 6: Example network

Spatio-temporal patterns Actually, in this case, instead of a model for a street network we need a model for the *event's (burglaries) network*. Such model was presented by T. Davis in his PhD Thesis (2015). This model can be firstly represented by means of two networks: one is based on the distance between two events (spatial proximity) and the other one is based on the time period between the events (temporal proximity). In these two networks the events are vertices but the corresponding sets of links are defined in different ways. If we take two threshold values D (spatial radius) and T (temporal radius) then

$$E_d^D = \{(i,j) \mid d_{ij} \leq D\},$$

and

$$E_t^T = \{(i,j) \mid 0 < t_{ij} \leq T\}.$$

Here, if two events occur in a given time period T, they are connected by a directed link from the earlier event to the later. This is the main difference: G_d^D is an undirected graph but G_t^T is a directed graph.

The undirected graph G_d^D and the directed graph G_t^T contain all the relevant information related to the set of events. By analysing both networks G_d^D and G_t^T, couples of events i and j which are close in space and time can be found. If the events are close in both space and time then the corresponding vertices are adjacent. One can now create an specifically event directed network G_{dt}^{DT}, of pairs which are close in space and time. This is the event network for the dataset, and it includes a space-time clustering analysis and it shows relations between events. This new network is the intersection of the spatial and temporal networks, that is,

$$E_{dt}^{DT} = \{(i,j) \mid (i,j) \in E_d^D \text{ and } (i,j) \in E_t^T\}.$$

The relationship between these three networks G_d^D, G_t^T, G_{dt}^{DT} is presented in Figure 7. Event network G_{dt}^{DT} is constructed using the other two, but it does not include the whole information for events from them. For example, if two events are not linked in G_{dt}^{DT}, it is impossible to know the reason for this disconnection, it could be because there is not a link in G_d^D, or G_t^T, or in neither of them.

In Figures 7 and 8 we provide an example with a simple set of event's data . We can see there the relation between the spatial network G_d^D, the temporal network G_t^T and the network of space-time pairs or events network G_{dt}^{DT}. The links of the event network G_{dt}^{DT} appear in the same position for both the spatial network G_d^D and the temporal network G_t^T.

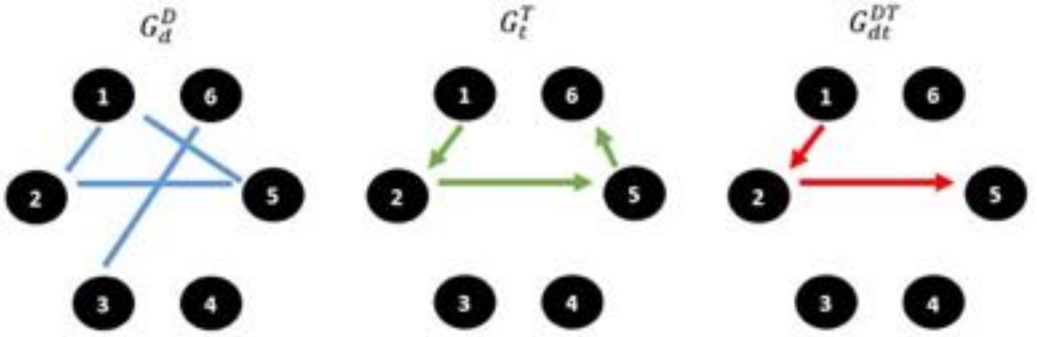

Figure 7: Original data, relationship between the three networks G_d^D, G_t^T and G_{dt}^{DT}

Figure 7 shows the connection for the original data while figure 8 shows how this can be changed with a simple permutation $\sigma(where 2 \leftrightarrow 6)$ of temporal data. This can be used in a Knox test with a Monte-Carlo approach.

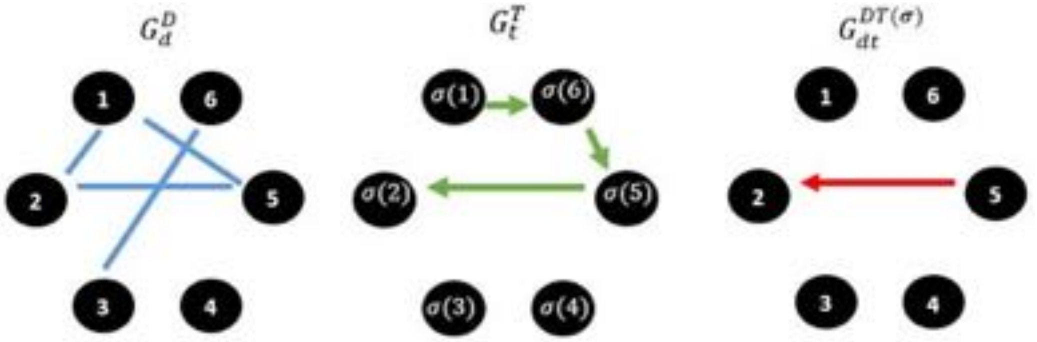

Figure 8: Relationship between the three networks under permutation σ of the temporal data

The Knox test is widely used in studies to detect space-time clustering or interactions between spatial and temporal distributions of a set of events. The origin of the test is in the study of childhood leukaemia. According to this concept, events are more likely to be close in space when they are close in time, and vice versa. The basis for the test is the concept of existing a close pair of events (close in time and close in space).

Acknowledgements

I. Serra acknowledges Generalitat de Catalunya for funding under grant 2014-SGR-1307 and the Spanish Government for funding under grant MTM2012-31118 . Her work is supported by a grant of the "la Caixa" Foundation on *Collaborative Mathematics* awarded to the Centre de Recerca Matemàtica. N. Folguera acknowledges the Spanish Ministry for Science and Innovation (MICINN) for funding under grant MTM2011-29342 and Generalitat de Catalunya for funding under grant 2014SGR1307. Her work is supported by a grant of the “la Caixa" Foundation on *Collaborative Mathematics* awarded to the Centre de Recerca Matemàtica. E. Costa-Miracle acknowledges the Spanish Ministry for Science and Innovation (MICINN) for funding under grant MTM2011-29342 and Generalitat de Catalunya for funding under grant 2014SGR1307. His work is supported by the BGSMath under grant MDM-2014-0445-04.

Bibliography

[1] J.T. Ornstein and R.A. Hammond. The Burglary Boost: A Note on Detecting Contagion Using the Knox Test. Journal of Quantitative Criminology (2106), 1–11.

[2] M. Egesdal, C. Fathauer, K. Louie, J. Neuman, G. Mohler, and E. Lewis. Statistical and stochastic modeling of gang rivalries in Los Angele. SIAM Undergraduate Research Online **3** (2010), 72–94.

[3] M.B. Short, M.R. D'Orsogna, V.B. Pasour, G.E. Tita, P.J. Brantingham, A.L. Bertozzi, and L.B. Chayes. A statistical model of criminal behavior. Math. Models Methods Appl. Sci. **18** (2008), 1249–1267.

[4] T.P. Davies and S.R. Bishop. Modelling patterns of burglary on street networks. Crime Science **2** (2013), 10.

[5] `http://nij.gov/topics/technology/maps/pages/crimestat.aspx`.

[6] `http://www.theguardian.com/cities/2014/jun/25/`.

MHD Equilibria of Tokamak Plasmas

Problem presented by
Alfredo Portone[1]

Report prepared by
Carles Barril[2], Àlex Haro[3], Marta Pellicer[4,7], Joan Solà-Morales[5]

Study group contributors
Carles Barril[2], Àlex Haro[3], Jesús Fernández-Sánchez[5], Giorgi Khimshiashvili[6], Marta Pellicer[4,7], Joan Solà-Morales[5]

1 Statement of the problems

The ITER project is an international project being developed in southern France. There, a world-wide consortium (China, the European Union, India, Japan, Korea, Russia and the United States) has launched the ITER initiative to design and build the world's largest tokamak, an experimental magnetic fusion device that has been developed to prove the feasibility of nuclear fusion as a large-scale and carbon-free source of energy. A tokamak is a device that confines a plasma by means of a toroidal magnetic field generated by external coils (see http://en.wikipedia.org/wiki/Tokamak). Actually, the term "tokamak", of Russian origin, stands for "toroidal chamber with magnetic coils". For stable equilibria, azimuthal (i.e., rotational) symmetry is required.

Fusion for Energy (F4E) is the European Union's Joint Undertaking for ITER and the Development of Fusion Energy. F4E is responsible, among others, for providing Europe's contribution to ITER project. This European Agency suggested the following two different problems to be discussed at the 115th European Study Group with Industry.

1.1 Problem 1: plasma boundary parametrization

The solution of the Grad-Shafranov equation [4], which is at the basis of tokamak plasma MHD equilibrium computations, in the fixed boundary formulation first requires the de-

---

[1] Fusion for Energy, Barcelona, Spain
[2] Universitat Autònoma de Barcelona, Bellaterra, Spain
[3] Universitat de Barcelona, Barcelona, Spain
[4] Universitat de Girona, Girona, Spain
[5] Universitat Politècnica de Catalunya, Barcelona, Spain
[6] Ilia State University, Tbilisi, Georgia
[7] Report co-ordinator: marta.pellicer@udg.edu

scription of the plasma boundary in terms of a few geometrical quantities. Typically, such quantities are R, a, k and δ, that is, the major and minor radius, the elongation and the triangularity of the toroidal plasma.

Limiter plasmas are characterized by a boundary that is a closed magnetic surface that is tangent to a material surface (poloidal or toroidal limiter). In cylindrical coordinates (r, φ, z), the flux does not depend on the φ angle (is axisymmetric). A common description for such type of boundary in the (r, z) section is given by the following parametrization (see [2] for details):

$$\begin{cases} r(\theta) = R + a\cos(\theta + \delta\sin(\theta)) \\ z(\theta) = k\sin(\theta), \end{cases}$$

where $\theta \in [0, 2\pi)$ represents the poloidal angle between the r-axis and the line connecting $(R, 0)$ and (r, z) (the generic plasma boundary point in the poloidal plane).

Divertor plasmas are characterized by a boundary that is not in contact with any material surface and contains a saddle point at which the boundary has a corner of 90 degrees. For such type of boundary (which is the most commonly used in burning plasmas) the parametrization above is no longer valid.

The **Fusion for Energy (F4E) problem** consists in finding a suitable family of curves (and depending on control parameters) whose only constraints in the (r, z) plane are:

(1) The curve must be tangent parallel to the z-axis (that is, *vertical* direction) at $(R_i, 0)$ and $(R_o, 0)$, the points of minimum and maximum radii of the curve, respectively. R_i and R_o should be specified by the user.

(2) The curve must contain a saddle point at (R_x, Z_x) where the branches cross at 90 degrees. (R_x, Z_x) should be specified by the user.

(3) The curve is not necessarily symmetric with respect to $z = 0$.

The curve should be given in terms of some (easy) geometric quantities.

1.2 Problem 2: plasma boundary control

The boundary of a tokamak plasma is controlled by acting on the currents flowing in the surrounding Poloidal Field (PF) coils. By solving the fixed boundary Grad-Shafranov equilibrium problem (see above) we easily establish the target flux function Ψ along the target plasma boundary Γ that must be matched by the currents flowing in the external PF coils. A typical example of such functions for different type of equilibria is shown in the figure below.

Perfect matching is possible only if the set of PF currents are placed along the plasma boundary itself [4], which is technically impossible. A common problem in tokamak engineering is therefore, to find a set of PF currents located on a different contour Γ^*, external to Γ, that match at best such target flux function Ψ while minimizing a weighted functional of error (JE) and cost (JC) (typically expressed in terms of magnetic energy, see [3, 4]).

The problem consists in providing an algorithm to compute the PF centers location and current along Γ^* to optimize a given functional J = JE + JC.

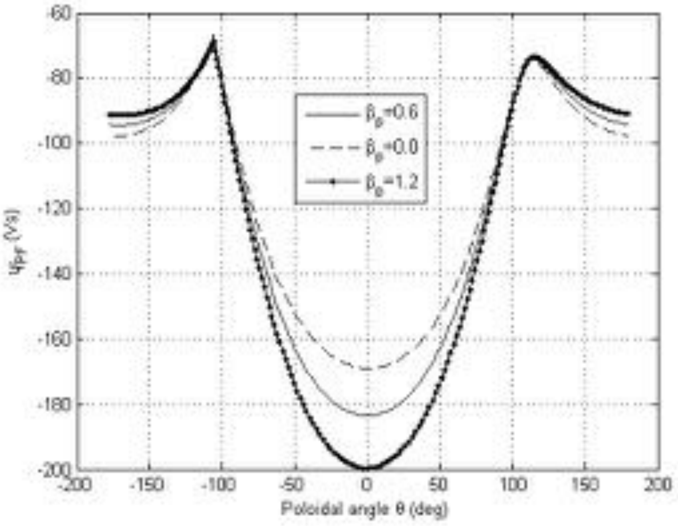

2 Problem 1: general remarks

We have proceeded to solve this problem mainly by two methods, that will be described in Sections 2 and 3 below. Before going into that, we give some general remarks. Without loss of generality, we assume a coordinate reference system where the cross point happens at $(a_0, b_0) = (0, 0)$. Also, instead of the geometrical quantities R, a, k, δ defined above, we are going to use the curve vertices coordinates (a_i, b_i), $i = 1, 2, 3$, (see Figure 1, right) in order to describe the main features of the curve. In particular, this means that the tangent lines at points (a_1, b_1) and (a_3, b_3) are vertical and the tangent line at point (a_2, b_2) is horizontal.

It is easy to relate these coordinates with the previous parameters. For instance:

$$a_1 = R + a, \ a_2 = 2R - 2a\delta, \ a_3 = R - a, \ b_2 = 2ak.$$

(in the case of $(a_0, b_0) \neq (0, 0)$, we would have the relation $\delta = (2R - a_2 - a_0)/(2a)$ and $2b = b_2 - b_0$ instead of the second and the fourth previous ones). We remark that as we are dealing with curves with a cross point, additional parameters may be used to define such a curve as, for instance, the slopes m_0, m_1 of the branches of the curve at this cross point.

To see how the methods we propose work, we are going to apply them to different sample problems, that we describe below. Notice that other combinations of the constraints we are going to give are also possible.

2.1 The balloon problem with a right corner (and fixed slopes)

In this problem we impose the following constraints (see Figure 1, left):

1) $(0, 0)$ is a cross point of the curve.
2) The curve is tangent at the vertical lines $x = a_1$ and $x = a_3$, and also to the horizontal one $y = b_2$.
3) We fix m_0, m_1, the right and left slopes at $(0, 0)$, respectively. We may have a right angle condition, that is $m_0 \cdot m_1 = -1$.

2.2 The F4E problem

In this problem we impose the following constraints (see Figure 1, middle):

1) $(0, 0)$ is a cross point of the curve.
2) The curve passes through (a_1, b_1) and (a_3, b_3). We may or may not impose $b_1 = b_3$.
3) Vertical tangencies at the previous points.
4) We fix m_0, m_1, the right and left slopes at $(0, 0)$, respectively. We may have a right angle condition, that is $m_0 \cdot m_1 = -1$.

The F4E problem with fixed height

In this problem we impose the same constraints as in the F4E problem 2.2, but also the following one:

5) the curve has horizontal tangent $y = b_2$.

The F4E problem with fixed top and height

In this problem we impose the same constraints as in the F4E problem 2.2, but also the following one (see Figure 1, right):

6) the curve has horizontal tangent $y = b_2$ at the point (a_2, b_2).

3 Method 1: polynomial interpolation

In this section we obtain solutions of the problem by parametric polynomial interpolation, that is, we are going to look for curves of the form

$$\big(x(t), y(t)\big) = \big(x_0 + x_1 t + x_2 t^2 + \cdots + x_m t^m,\ y_0 + y_1 t + y_2 t^2 + \cdots + y_n t^n\big), \quad t \in [0, 1]$$

whose coefficients will be determined by the constraints of the problem. Observe that the degrees of the polynomials m, n will depend on the amount of constraints we impose on the definition of the curve.

As we are going to see, the constraints we will be dealing with can be written as linear equations on the previous polynomial coefficients. Hence, finding the polynomials will simply consist of finding the solution of a linear system of equations.

First of all, and without loss of generality, we are going to assume that the cross point $(0, 0)$ is achieved at $t = 0$ and $t = 1$. Therefore, we immediately obtain that

$$x_0 = y_0 = 0,$$

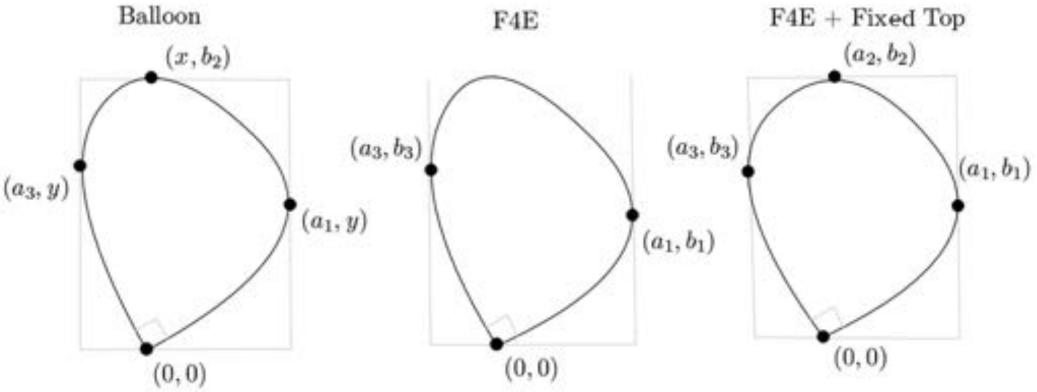

Figure 1: Diagrams of three different example problems. From left to right, the balloon problem with a right corner, the F4E problem and the F4E with a fixed top problem.

$$
\begin{aligned}
x_1 + \ldots + x_m &= 0, \\
y_1 + \ldots + y_n &= 0.
\end{aligned}
$$

Apart from the previous cross point condition, the constraints on the vertices conditions at points (a_i, b_i), $i = 1, 2, 3$, will be imposed at times t_1, t_2, t_3, respectively. This times can be specified by the user. Actually, we can obtain many interpolating curves by using t_i as tunning parameters to fit the target curve.

The constraints on the vertices (and, hence, the corresponding linear equations on the coefficients) are from the following three types:

(i) the curve has to pass through a given point (a_i, b_i) at a given time $t = t_i$, that is, $(x(t_i), y(t_i)) = (a_i, b_i)$. Imposing this condition leads to the following linear equations for the coeficients x_i, y_j:

$$
\begin{aligned}
x_1 t_i + x_2 t_i^2 + \cdots + x_m t_i^m &= a_i, \\
y_1 t_i + y_2 t_i^2 + \cdots + y_n t_i^n &= b_i.
\end{aligned} \tag{1}
$$

(ii) The curve has to be tangent to the vertical line $x = a_i$ or the horizontal one $y = b_i$ at $t = t_i$. Imposing these conditions, we obtain $x(t_i) = a_i$ and $x'(t_i) = 0$ in the first case, that is:

$$
\begin{aligned}
x_1 t_i + x_2 t_i^2 + \cdots + x_m t_i^m &= a_i, \\
x_1 + 2x_2 t_i + \cdots + m x_m t_i^{m-1} &= 0
\end{aligned}
$$

or $y(t_i) = b_i$ and $y'(t_i) = 0$ in the second one, that is

$$
\begin{aligned}
y_1 t_i + y_2 t_i^2 + \cdots + y_n t_i^n &= b_i, \\
y_1 + 2y_2 t_i + \cdots + n y_n t_i^{n-1} &= 0.
\end{aligned}
$$

In the case of having a tangency condition exactly at the point (a_i, b_i), we would combine (1) with the corresponding previous conditions on the derivatives.

(iii) Slopes or angle condition. We recall that the slope of the curve at a certain point $(x(t), y(t))$ is simply $y'(t)/x'(t)$. In particular, for $t = 0$ and $t = 1$, the slopes m_0, m_1 satisfy the equations

$$m_0 x_1 - y_1 = 0$$

and

$$m_1 (x_1 + 2x_2 + \cdots + m x_m) - (y_1 + 2y_2 + \cdots + n y_n) = 0,$$

respectively. Observe also that the angle at $(0, 0)$ will be of 90 degrees if $m_0 \cdot m_1 = -1$. More generally, an angle α_0 at $(0, 0)$ would be obtained by imposing the condition:

$$\cos \alpha_0 = \frac{-1 - m_0 m_1}{\sqrt{(1 + m_0^2)(1 + m_1^2)}}.$$

Remark 3.1. It is worth to say that other types of interpolation can be used (such as splines), that may be also convenient from a numerical point of view. We have to say that in this case we would obtain a piecewise parametrization.

Also, when the only conditions are those requiring that the curve passes through a set of given points, there are well-known ways and methods to obtain the interpolating polynomial more efficiently.

To illustrate the method, we are going to state and solve different problems, that have already been described in Section 2.

3.1 The balloon problem with a right corner (and fixed slopes)

This problem is described in 2.1 of Section 2, but we add here the times t_i where the corresponding constraints must be fulfilled.

1) $(0, 0)$ is a cross point and the curve passes through it at $t = 0$ and $t = 1$.
2) Tangency conditions at $x = a_1$, $y = b_2$, $x = a_3$ at times t_1, t_2, t_3 respectively.
3) Fixed slopes m_0, m_1 at $(0, 0)$ when $t = 0$ and $t = 1$. We may have a right angle condition, that is $m_0 \cdot m_1 = -1$.

In this case, $(x(t), y(t))$ can be obtained as polynomials both of degree 5 if we include the slope conditions as conditions to determine the coefficients of $y(t)$. In the second plot of Figure 2 we can see an example of this problem solve by method 1.

3.2 The F4E problem

This problem is described in 2.2 of Section 2, but we add here the times t_i where the corresponding constraints must be fulfilled. In this problem we impose the following constraints:

1) $(0, 0)$ is a cross point and the curve passes through it at $t = 0$ and $t = 1$.
2) The curve passes through (a_1, b_1) and (a_3, b_3) at $t = t_1, t = t_3$ respectively. We may or may not impose $b_1 = b_3$.
3) Vertical tangencies at the previous points at $t = t_1, t = t_3$ respectively.

4) Fixed slopes m_0, m_1 at $(0,0)$ when $t = 0$ and $t = 1$. We may have a right angle condition, that is $m_0 \cdot m_1 = -1$.

In this case, $(x(t), y(t))$ can be obtained as polynomials both of degree 5 if we include the slope conditions as conditions to determine the coefficients of $y(t)$. In the third plot of Figure 2 we can see an example of this problem.

The F4E problem with fixed top and height

This problem is described in 2.2 of Section 2. The times times t_i where the corresponding constraints must be fulfilled are the previous ones for the F4E problem, and also

5) the curve passes through (a_2, b_2) and has horizontal tangent at this point at $t = t_2$.

In this case, $(x(t), y(t))$ can be obtained as polynomials of degree 6 and 7, respectively, if we include the slope conditions as conditions to determine the coefficients of $y(t)$. See Figure 2, right, for an example of this problem.

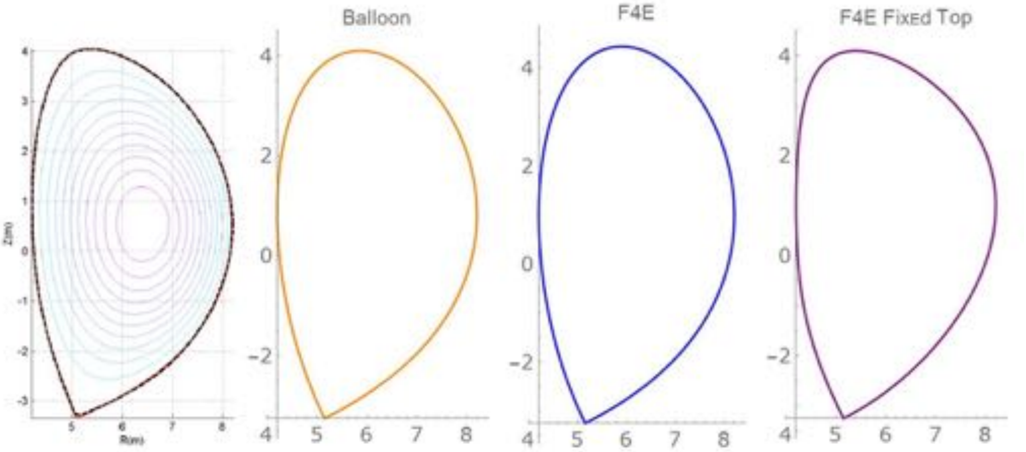

Figure 2: Simulation of method 1 (polynomial interpolation) for the three different problems described above (second, third and fourth plots). Compare with the left figure which is a representation of the plasma given in [3].

4 Method 2: level curves

Motivated by the level curves of a Hamiltonian with a cubic potential energy, our approach in this section will consist of finding an implicit representation of the curve as the zero level set of a cubic Hamiltonian. That is, finding a cubic function, whose general form is

$$H(x,y) = \alpha_{00} + \alpha_{10}x + \alpha_{01}y + \alpha_{20}x^2 + \alpha_{11}xy + \alpha_{02}y^2 + \alpha_{30}x^3 + \alpha_{21}x^2y + \alpha_{12}xy^2 + \alpha_{03}y^3$$

such that its zero level curve ($\Gamma_0 = \{(x,y) \in \mathbb{R}^2,\ H(x,y) = 0\}$) fits the target conditions.

Using this approach we would also obtain the set of level curves $\Gamma_c = \{(x,y) \in \mathbb{R}^2,\ H(x,y) = c\}$ and that these curves would be generically regular when $c \neq 0$.

Observe that as $(0,0)$ must be a saddle point, we immediately obtain that $\alpha_{00} = \alpha_{10} = \alpha_{01} = 0$ (as $H(0,0) = H_x(0,0) = H_y(0,0) = 0$). Observe also that we can then assume $\alpha_{20} \neq 0$ without loss of generality to avoid that the vertical axis is one of the saddle axis. So, we can divide all the coefficients by α_{20} and, hence, the cubic we are looking for has the general form

$$H(x,y) = x^2 + \alpha_{11}xy + \alpha_{02}y^2 + \alpha_{30}x^3 + \alpha_{21}x^2y + \alpha_{12}xy^2 + \alpha_{03}y^3. \tag{2}$$

In this curve we have six coefficients to be fixed. This will be done imposing up to six constraints on the problem. A natural way to fix all of them is to impose that the vertices of the curve are (a_i, b_i), $i = 1, 2, 3$. However, in general we will not obtain a right angle at $(0,0)$. A way of getting it could be not fixing one of the vertices (for instance, (a_2, b_2)) and use it as a tunning parameter to achieve the right angle condition, as we will see below.

Although the curve (2) is given in an implicit form, there exists a classical method to obtain its parametrization. Consider the sheaf of straight lines passing through the origin $(0,0)$, that is, $y = tx$. Observe that t has a geometrical meaning: it represents the slope with respect to the horizontal axis at the point $(0,0)$. The method consists in observing that each of these lines intersects at three points with the cubic. But, as $(0,0)$ is a cross point of the curve, two of these points are $(0,0)$, so the third intersection point gives us a parametrization of the curve:

$$x(t) = -\left(\frac{\alpha_{02}t^2 + \alpha_{11}t + 1}{\alpha_{03}t^3 + \alpha_{12}t^2 + \alpha_{21}t + \alpha_{30}}\right), \quad y(t) = t\,x(t)$$

with $t \in [m_1, m_0]$, where m_0, m_1 stand for the right and left slopes at $(0,0)$ with respect to the horizontal axis, respectively:

$$m_0 = \frac{2}{-\alpha_{11} + \sqrt{\alpha_{11}^2 - 4\alpha_{02}}},\ m_1 = \frac{2}{-\alpha_{11} - \sqrt{\alpha_{11}^2 - 4\alpha_{02}}}. \tag{3}$$

Notice that

$$\alpha_{11} = -\left(\frac{m_0 + m_1}{m_0 m_1}\right),\ \alpha_{02} = \frac{1}{m_0 m_1}. \tag{4}$$

The right angle case would be when $m_0 \cdot m_1 = -1$, that is, $\alpha_{02} = -1$.

The type of constraints we may have are the following:

(i) the curve has to pass through a given point (a_i, b_i), that is:

$$H(a_i, b_i) = 0$$

which is a linear equation on the coefficients α_{ij}.

(ii) Tangency conditions. Observe that if the tangency conditions happen at a particular point (a_i, b_i), then we have

$$H(a_i, b_i) = H_y(a_i, b_i) = 0$$

for a vertical tangent or

$$H(a_i, b_i) = H_x(a_i, b_i) = 0$$

for an horizontal one, which are linear equations on the coefficients.

If the curve has to be tangent to the vertical line $x = a_i$ or the horizontal one $y = b_i$, it must be fulfilled that

$$H(a_i, y) = H_y(a_i, y) = 0 \ \text{ or } H(x, b_i) = H_x(x, b_i) = 0, \tag{5}$$

respectively. But observe that in these equations there are x or y as new unknowns (if we knew the exact points where these tangencies occur, then these would be linear equations on the coefficients). Hence, a better way to think these generic vertical or horizontal tangencies is through the discriminant of the cubic. More concretely, if the curve has to be tangent to the vertical line $x = a_i$, this would happen at a double root of the y-cubic function $H(a_i, y)$. So, $H(a_i, y)$ would be a cubic y-polynomial with zero discriminant (to assure this double root happen). Hence, the conditions (5) could be replaced by the corresponding zero discriminant conditions, which are nonlinear equations of the coefficients.

(iii) Slope conditions. We have seen in (3) the relation between the slopes m_0, m_1 at $(0, 0)$ in terms of the coefficients of the cubic function H. Recall that the case of a right angle at $(0, 0)$ corresponds to $\alpha_{02} = -1$. In the case of imposing given slopes, the coefficients α_{11} and α_{02} are fixed by (4).

As we have said, in the general form (2) of the cubic we are looking for there are six coefficients to be fixed. So, to fix all of them we would need exactly six appropriate conditions on the curve. In other words, in problems with less constraints (such as, for instance, the balloon problem with a right corner or the F4E problem) we will obtain a cubic curve of the form (2) but with some free coefficients. These coefficients can be turned into zero or we can use them as tunning parameters to achieve the desired curve.

To illustrate this method, we are going to apply it to the F4E problem described in Section 2 and see how the free parameters can be used to fit the target curve.

4.1 The F4E problem

Following the requirements of the F4E problem (see 2.2 in Section 2), the first condition to be achieved is a right angle at $(0, 0)$. This condition yields to

$$H(x, y) = x^2 + \alpha_{11}xy - y^2 + \alpha_{30}x^3 + \alpha_{21}x^2y + \alpha_{12}xy^2 + \alpha_{03}y^3.$$

Fixing the two lateral vertices at (a_1, b_1) and (a_3, b_3) corresponds to four linear equations of the remaining coefficients. Hence, we will have a free parameter, that can be chosen to be, for instance, α_{30}. This means that we can choose it either to be zero or we can use it as a tunning parameter to achieve the target curve.

The F4E problem with fixed height

Following the previous approach, we can adjust α_{30} in order to get a desired height b_2, that is, to get an horizontal tangency at $y = b_2$. In Figure 3 (right) we can see the relation between this α_{30} and b_2. A simulation of this second method for a F4E problem can be seen in Figure 3 (middle).

Another point of view for solving the F4E problem with fixed height is imposing the tangency condition at $y = b_2$ as a discriminant condition, getting an extra cubic equation for α_{30}.

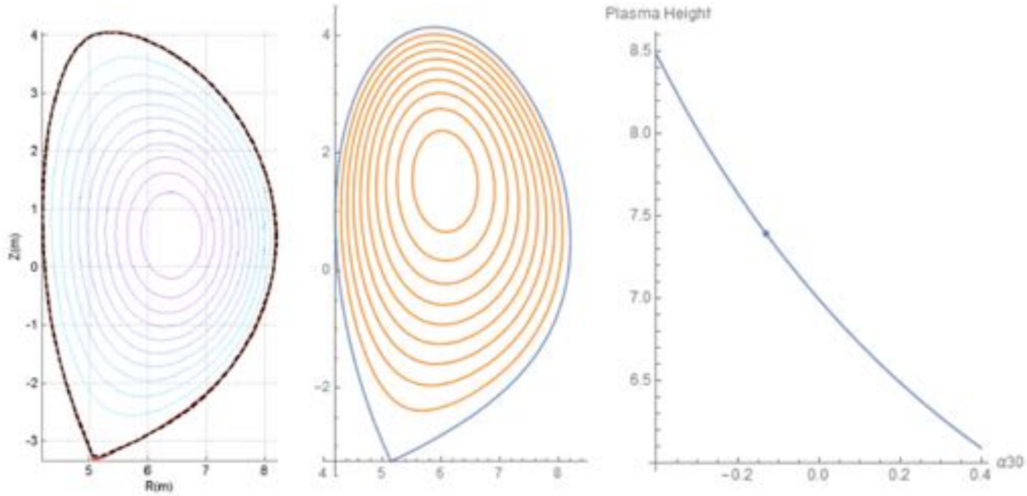

Figure 3: In the middle, simulation of method 2 applied to the F4E problem. See also the different level curves of the cubic Hamiltonian and compare with the left figure which is a representation of the plasma given in [3]. The right curve shows the relation between the plasma height b_2 and the free parameter α_{30} (the point corresponds to the value used in the simulation, that has been chosen to fit the desired height of the plasma, according to its representation given in left figure).

In conclusion, using an implicit cubic representation of the curve allows a maximum of six constraints. If we want to impose more constraints, we should use a higher order implicit polynomial representation. For instance, an implicit quartic representation would add the possibility of five more free parameters to be adjusted. Notice, however, that in this case we generally do not have a rational parametric representation of the curve but an irrational one.

5 Some ideas for Problem 2

In Problem 2 presented by F4E, one is asked to find the currents along the exterior coils to produce a scalar field Ψ on the boundary Γ of the plasma region that matches a given target function. This target scalar field is supposed to be previously found as a solution of a Grad-Shafranov equation in a fixed domain (see subsection **??** for details).

Though important contributions were made in [3], the problem seems to be quite involved, but it has many of the characteristics of the next problem, that we suggest because it is simpler and perhaps suitable for a mathematical warm-up in the stated direction.

Let $\Omega \subset \mathbb{R}^2$ be an open set with a simple boundary Γ. It is known (for example, see [1] for details) that every harmonic function $u(\vec{x})$ in Ω that is continuous up to Γ can be represented as the resultant of a continuous distribution of double layer dipoles oriented in the direction of the exterior normals to Γ and with intensities $\mu(\vec{\xi})$, that is

$$u(\vec{x}) = -\frac{1}{2\pi}\int_{\Gamma}\mu(\vec{\xi})\frac{\partial}{\partial\vec{\nu}_{\vec{\xi}}}\ln|\vec{\xi}-\vec{x}|d\ell_{\vec{\xi}}.$$

To get some intuition, one can consider the case where Γ is a circle centered at $(0,0)$. In this case,

$$\frac{\partial}{\partial\vec{\nu}_{\vec{\xi}}}\ln|\vec{\xi}-\vec{x}| = \frac{\vec{\xi}\cdot(\vec{\xi}-\vec{x})}{|\vec{\xi}-\vec{x}|^3}.$$

It is known that the density function $\mu(\vec{x})$ is the solution of the following Fredholm integral equation of the second kind:

$$\mu(\vec{x}(s)) - \frac{1}{\pi}\int_{\Gamma}\mu(\vec{x}(t))\frac{\partial}{\partial\vec{\nu}_{\vec{\xi}}}\ln|\vec{\xi}(s)-\vec{x}(t)|\ dt = -2u(\vec{x}(s)),$$

where s and t are counterclockwise arc-length coordinates along Γ.

Let now $\Omega_1 \subset \Omega_2 \subset \mathbb{R}^2$ be two open sets with simple boundaries Γ_1 and Γ_2 respectively. What it is not true is that every such function $u(\vec{x})$ defined in Ω_1 can be represented as a continuously distributed double-layer potential along Γ_2. This can hold in some particular cases, but in general it is an ill-posed problem. To see if this function $u(\vec{x})$ coincides with the function $v(\vec{x})$ defined by a double-layer potential distribution along Γ_2 it would be enough to see that they coincide on Γ_1.

Even worse is the discretized problem, where the dipoles are a finite number n of point-dipoles distributed along Γ_2, namely at the points $\vec{\xi}_1, \vec{\xi}_2 \ldots \vec{\xi}_n \in \Gamma_2$ with intensities (moments) $\mu_1, \mu_2 \ldots \mu_n$ (directed along the unit exterior normals of Γ_2), and the integral is substituted by a finite sum.

But even if this problem has in general no solution, we can ask ourselves to minimize the error when approximating in such a way a function $u(\vec{x})$ in Ω_1, or more precisely on Γ_1:

Problem A. Given m points $\vec{x}_1, \vec{x}_2 \ldots \vec{x}_m$ in Γ_1 and n (fixed) points $\vec{\xi}_1, \vec{\xi}_2 \ldots \vec{\xi}_n \in \Gamma_2$, find the intensities $\mu_1, \mu_2 \ldots \mu_n$ that minimize

$$\sum_{i=1}^{m}(v(x_i) - u(x_i))^2$$

where

$$v(\vec{x}) = \sum_{j=1}^{n}\mu_j\frac{\partial}{\partial\vec{\nu}_{\vec{\xi}}}\ln|\vec{\xi}_j - \vec{x}|.$$

Problem B. Same problem as before, but letting the locations $\vec{\xi}_1, \vec{\xi}_2 \ldots \vec{\xi}_n \in \Gamma_2$ to be also variable.

Acknowledgements

The authors thank Alfredo Portone and the European Agency Fusion for Energy for proposing this problem to the 115th European Study Groups with Industry. The authors would also like to thank Jesús Fernández and Giorgi Khimshiashvili for their helpful discussions on the problem.

This work is partially supported by the Spanish grants MTM2014-52402-C3-1-P (J. Solà-Morales), MTM2014-52402-C3-2-P (C. Barril) and MTM2014-52402-C3-3-P (M. Pellicer). Also, C. Barril, M. Pellicer and J. Solà-Morales are part of the Catalan research group 2014-SGR-1083, and M. Pellicer is also partially supported by MPC UdG 2016/047 (U. de Girona, Catalonia). À. Haro acknowledges financial support from the Spanish grant MTM2015-67724-P and the Catalan grant 2014-SGR-1145.

Bibliography

[1] A.V. Bitsadze. Equations of Mathematical Physics. Mir Publishers, Moscou (1980).

[2] R.L. Miller, M.S. Chu, J.M. Greene, Y.R. Lin-Liu, and R.E. Waltz. *Noncircular, finite aspect ratio, local equilibrium model.* Physics of Plasmas **5** (1998), 973–978.

[3] A. Portone. Magnet system optimization in tokamak engineering. Decision and Control (CDC), 2012 IEEE 51st Annual Conference on (4328–4334). IEEE.

[4] T. Takeda and S. Tokuda. Computation of MHD Equilibrium of Tokamak Plasma. J. Comput. Phys. **93** (1991), 1–107.

Material Wait Time Problem

Problem presented by
Joan Jané[1]

Report prepared by
Ernest Benedito[2,7]

Study group contributors
Unai Aldasoro[3], Xavier Bardina[4], Ernest Benedito[2,7], Alejandra Cabaña[4], Gemma Colldeforns[5], Roberto de la Cruz[5], Fernando Martínez[2], Francisco Javier Muñoz[2], David Portabella[6], Miguel Romero[6]

1 Statement of the problem

An efficient Supply Chain Management must provide a methodology for setting the best possible plans, procuring the appropriate amount of material to support those plans, and making up-front business decisions on the costs of inventory versus material wait time (MWT), service level to MWT objectives, future demand uncertainty, part lead times, and part delivery uncertainty.

In this context, Hewlett-Packard (HP) is facing with the problem of determining the required inventory position (Q) to meet a certain service level (SL) within a specific MWT. Specifically, HP wants to study the relationship between these three variables: Q, SL and MWT. To this end, the problem under consideration is formulated as follows:

Consider a factory building some arbitrary product to meet customer demand. Since future demand is always an uncertainty, planning and procurement must wrestle with the task of setting plans at the right level and procuring the appropriate material. The organization strives to run the factory between two equally unattractive scenarios: not enough inventory and long material wait times (MWTs), or excessive inventory but meeting

---

[1] Hewlett Packard, Sant Cugat, Spain
[2] Universitat Politècnica de Catalunya, Barcelona, Spain
[3] Basque Center for Applied Mathematics, Bilbao, Spain
[4] Universitat Autònoma de Barcelona, Bellaterra, Spain
[5] Centre de Recerca Matemàtica, Barcelona, Spain
[6] Universitat de Barcelona, Barcelona, Spain
[7] Report co-ordinator: ernest.benedito@upc.edu

MWT goals. In fact, more than one organization has found itself with the worst of both worlds-huge inventories and poor MWTs.

The problem is defined under de following assumptions:

- Assumption 1: Customer demand. The demand in each period is stochastic, modelled as a series of IID variables with normal distributions. The series is assumed to be stationary with mean and standard deviation μ, σ respectively.
- Assumption 2: Inventory policy. The customer demand is fulfilled by pulling from an inventory of parts (make-to-stock production strategy). The inventory is managed through a Periodic Review Order-Up-To Point policy with review period R, and Order-Up-To point Q. With the periodic review system, the company determines the quantity of product on hand at specified, fixed-time intervals (R) and places an order to the supplier for an amount equal to the Order-Up-To point (Q), minus the inventory position. Inventory position is defined as the on-hand plus on-order (orders placed to the supplier and not received).
- Assumption 3: Customer demand order fulfilment. Strict FIFO with partial order fulfilment/ partial inventory allocation. In this case, material is allocated to an order, even if there aren't enough inventories to fulfil the order as a whole.
- Assumption 4: Replenishment lead time. The replenishment action has a stochastic Lead Time $L(t)$ which is stationary and IID from a normal, lognormal and gamma distribution with mean and standard deviation l, s. The supplier follows a FIFO order fulfilment.

Performance indicators objectives: Service Level $\geq$ SL, Material Wait Time $\leq$ MWT.

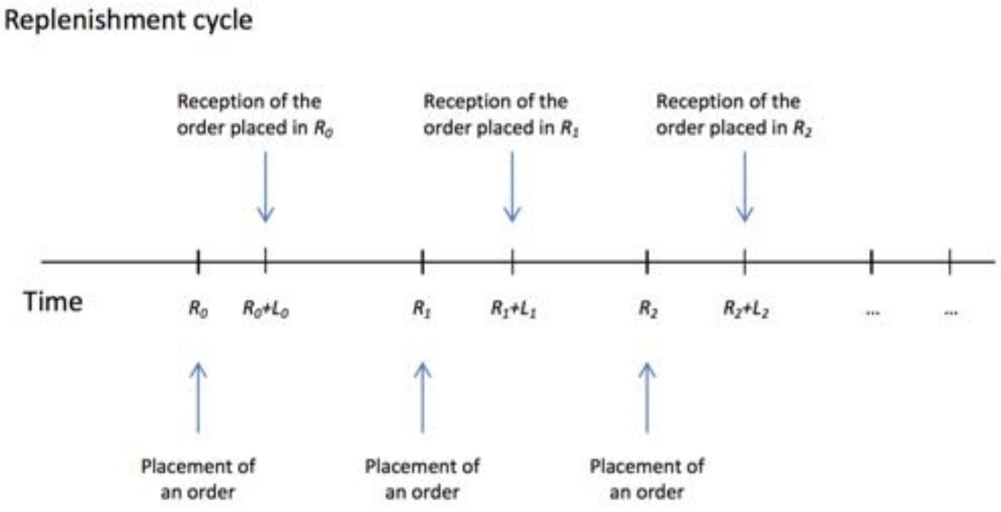

The objectives of the present work are:

- Calculate the probability P(T $\leq \tau$) where T is the random variable describing the time an order has to wait until material becomes available if the required material (components or line items) are not immediately available.

- Calculate relationships between the following three variables: MWT (Material Wait Time, periods), SL (Service Level, fraction of demand met within MWT), Q (Order-Up-To point) where P(T $\leq$ MWT) $\geq$ SL.
- Make an assessment of the impact the distribution assumption of demand and lead time has.
- Have some sort of tool (EXCEL preferably) encapsulating the math.

2 Model formulation

To meet the objectives of the work we must define model that allows us to calculate the time since a customer demand order is placed and the order is satisfied. This time depend on the on-hand inventory of product (quantity of product available in the stock) at the time of the customer order is allocated.

The on-hand product inventory may change over time depending, mainly, on the quantities of product demanded by the customers and on the product received from the supplier. Considering assumption 1, the customer demand can be modeled as a stochastic process with known probability distributions. Regarding the product received from the supplier, it depends on when the company allocates the orders to the supplier, the quantity of each order and the fulfilment lead time of the supplier. From assumption 2, the orders to the supplier are placed at specified and fixed-time intervals. Without loss of generality, let the supplier orders are placed at time 1, 2, 3, ... From assumption 4, the supplier lead time can be modelled as random variables with known probability distributions.

Also from assumption 2, the quantity ordered to the supplier depends on the order-up-to point Q and the inventory position at the time of ordering to the supplier. The inventory position is defined as the on-hand product inventory plus the orders placed to the supplier and not received.

Therefore the model must clarify the relation between the on-hand product inventory, the customer demand and the supplier demand orders.

The model proposed has the elements defined as follows:

- Q: Order-Up-To point.
- $D(t)$: Customer demand up to time t, in units of product.
- $h(t)$: On-hand inventory of product, in units, at time t, $t \in \mathbb{R}^+$.
- $p(t)$: Units of product ordered to the supplier allocated before t and not received at time t, $t \in \mathbb{R}^+$.
- $r(t)$: Units of product received from the supplier up to time t, $t \in \mathbb{R}^+$
- a_k: Units of product ordered to the supplier at time k, $k \in \mathbb{Z}^+$. Assume without loss of generality that the review period $R = 1$.
- L_k: Lead time since k, the time when an order is placed to the supplier and the supplier fulfil the order, $k \in \mathbb{Z}^+$.

Suppose that $h(0) = 0$, $p(0) = 0$ i $r(0) = 0$.

With these definitions we want to write the on-hand inventory product as a function depending on $Q, D(t)$ i L_k.

Taking into account assumption 2, the supplier order allocated at time $k \in \mathbb{Z}R^+$, is

$$a_k = Q - h(k) - p(k) \tag{1}$$

And from assumption 3:

$$h(t) = r(t) - D(t) \tag{2}$$

And form assumption 4, we obtain:

$$r(t) = \sum\nolimits_{\{k\in\mathbb{Z}^+ | k+L_k \le t,\, k<t\}} a_k \tag{3}$$

$$p(t) = \sum\nolimits_{\{k\in\mathbb{Z}^+ | k<t\}} a_k - r(t) \tag{4}$$

Where L_k is the lead time of the supplier order allocated at time k.

Combining (2), (4) and (1) the quantities of the orders allocated to the supplier can be written as:

$$\begin{aligned} a_0 &= Q \\ a_k &= D(k) - D(k-1), \quad k = 1, 2, 3, \ldots \end{aligned}$$

And with the supplier FIFO order fulfilment in assumption 4, we have that $k + L_k \le k + 1 + L_(k+1)$, $k \in \mathbb{Z}^+$. Then, the orders received form the supplier and the on-hand inventory at time t, can be written as:

$$r(t) = \begin{cases} 0 & t < L_0 \\ Q + D(k_t - 1) \ge L_0 & t \ge L_0 \end{cases} \tag{5}$$

$$h(t) = \begin{cases} -D(t) & t < L_0 \\ Q - [D(t) - D(k_t - 1)] & t \ge L_0 \end{cases} \tag{6}$$

where

$$k_t \equiv \min\{k \in \mathbb{Z}^+ | t < k + L_k\}. \tag{7}$$

With this result, in the next section we calculate the time since a customer demand order is placed and the order is satisfied.

3 Probability distribution of $\boldsymbol{T}$

We are interested in studying the time elapsed since a customer demand order is allocated and the order is fulfilled.

Let t be the time when a customer demand order is allocated and T_t the time elapsed since the order is allocated up to the demand order is fulfilled. Taking into account assumption 3 (FIFO policy for customer demand fulfilment) we have that:

$$T_t = 0 \text{ iif } h(t) = Q - D(t) + D(k_t - 1) > 0, \quad t \ge L_0.$$

and then, the probability of $T_t = 0$ is:

$$\begin{aligned} P(T_t = 0) &= \sum_{(k=0)}^{\infty} P\big(Q - D(t) + D(k) > 0 \mid k_t = k+1\big) \cdot P(k_t = k+1) \\ &= \sum_{(k=0)}^{\infty} P\big(D(t) - D(k) < Q\big) \cdot P\big((L_k \le t - k) \wedge (L_{k+1} > t - k - 1)\big) \end{aligned}$$

$0 < T_t \leq \tau$ iff $h(t) \leq 0$ and there exists $s \in (t, \tau]$ such that $r(s) - r(t) + h(t) > 0$.

In order to calculate the probability of $0 < T_t \leq \tau$ we need to know when a customer order will be served. Suppose that a customer order arrive at time t and $h(t) \leq 0$, then the order is served at $m_t + L_{m_t})$, obtained from the following proposition:

Proposition. *Given* $t \in \mathbb{R}^+$ *such that* $h(t) \leq 0$ *then,*

- $r(s) - r(t) + h(t) \leq 0, \quad \forall s \in [t, m_t + L_{m_t})$
- $r(m_t + L_{m_t}) - r(t) + h(t) > 0$

where $m_t \equiv \ min \ \{k \in \mathbb{Z}^+ \mid Q - D(t) + D(k) > 0\}$.

Proof. Given $s \geq t$, regarding (5) and (**??**) we have:

$$r(s) - r(t) + h(t) = \begin{cases} -D(t) & s < L_0 \\ Q - D(t) + D(k_s - 1) & s \geq L_0. \end{cases}$$

Taking into account the definition of m_t:

- $r(s) - r(t) + h(t) \leq 0$ if $k_s \leq m_t$
- $r(s) - r(t) + h(t) > 0$ if $k_s \geq m_t + 1$.

From (7) we have that if $s = k + L_k$, $(k \in \mathbb{Z}^+)$ then $k_s = k + 1$ and $k_s \leq k$ if $s < k + L_k$. Then, $s = m_t + L_{m_t}$ is the lowest s such that $k_s = m_t + 1$. $\square$

With this proposition we have that

$$\begin{aligned} P(0 < T_t \leq \tau) &= P\big(t < m_t + L_{m_t} \leq t + \tau\big) \\ &= \sum_{k=0}^{\infty} P\big(t < k + L_k \leq \tau + t \mid m_t = k\big) \cdot P(m_t = k) \\ &= \sum_{k=0}^{\infty} P\big(t - k < L_k \leq t + \tau - k\big) \\ &\qquad \cdot P\big((Q - D(t) + D(k) > 0) \wedge (Q - D(t) + D(k-1) \leq 0)\big). \end{aligned}$$

Taking into account assumption 4 (L_k, $k \in \mathbb{Z}^+$ are iid random variables) and that $P(D(t) - D(s) < Q) = P(D(t - s) < Q)$, $\forall s, t$ (from assumption 1, $D(t)$ is normally distributed):

$$P(T_{n+u} = 0) = \sum_{k=0}^{n} P\big(D(k+u) < Q\big) \cdot P(L \leq k + u) \cdot [1 - P(L \leq k + u - 1)] \tag{8}$$

$$\begin{aligned} &P\big(0 < T_{n+u} \leq \tau\big) \\ &= \sum_{k=-u-\tau}^{n} \big[P(L \leq k+u+\tau) - P(L \leq k+u)\big] \cdot P\big((D(k+u) < Q) \wedge (D(k+u+1) \geq Q)\big) \end{aligned} \tag{9}$$

Where $t = n + u$, with $n \in \mathbb{Z}^+$ and $u \in [0, 1)$ and L is random variable identically distributed as L_k, $\forall k \in \mathbb{Z}^+$ (i.e., $P(L \leq x) = P(L_k \leq x), \forall x \in \mathbb{R}$).

It can be assumed that the lead time is upper bounded. Let $L_{\max}$ be the best upper bound, then

$$1 - P\big(L \leq k + u - 1\big) = 0, \quad \forall k \geq L_{\max} - 1$$

$$P\big(L \leq k + u + \tau\big) - P\big(L \leq k + u\big) = 0, \quad \forall k \geq L_{\max}.$$

And then, (8) and (9) can be rewritten as:

$$P(T_{n+u} = 0) = \sum_{k=0}^{\min\{n, L_{\max}-1\}} P\big(D(k+u) < Q\big) \cdot P\big(L \leq k+u\big) \cdot \big[1 - P(L \leq k+u-1)\big]$$

$$P\big(0 < T_{n+u} \leq \tau\big) = \\ \sum_{k=-u-\tau}^{\min\{n, L_{\max}\}} \big[P(L \leq k+u+\tau) - P(L \leq k+u)\big] \cdot P\big((D(k+u) < Q) \wedge \big(D(k+u+1) \geq Q\big)\big)$$

Observe that for $t \geq L_{\max}$, $P(T_{n+u} = 0)$ and $P(0 < T_{n+u} \leq \tau)$ only depends on u, and does not depend on n. Once obtained probability distribution of T_t, we can calculate the probability distribution of T, the lead time of a customer order. We are interested in the orders placed after time $L_{\max}$.

Let $t_1 \leq t_2 \leq \cdots \leq t_i \leq \cdots$ be the times when the customer orders are allocated. Let put $t_i = n_i + u_i$; $n_i \in \mathbb{Z}^+$; $u \in [0, 1)$.

In order to calculate $P(T \leq \tau)$, we need some additional assumptions on the time when the customer allocates his order. We explain the results in two cases:

Case 1. The customer places the orders at times $t_i = n_i + u$, $\forall i$ (i.e., $u_1 = u_2 = \cdots = u$). In this case $P(T \leq \tau) = P(T_(L_{\max+u}) \leq \tau)$, $\forall \tau, u$.

Case 2. The customer place the orders in a way such that the inter arrival time of two successive orders $(t_{i+1} - t_i)$ is a random variable that follows an exponential distribution. We assume that u_i can be modelled as a random variable U that follows a uniform distribution $U[0, 1]$. In this case

$$P(T \leq \tau) = E\big[P(T_{L_{\max}+u}) \leq \tau \mid U = u)\big] = \int_0^1 P\big(T_{L_{\max}+u} \leq \tau\big) du.$$

The expressions of the probability distribution of T have been implemented in Microsoft Excel VBA.

4 Results

We studied the system in 4 different cases. The objective is to calculate the relationships between MWT, SL and Q where $P(T \leq MWT) \geq SL$.

In each case, it is supposed that the daily demand and lead time follow Normal distributions, and that the customer place the orders uniformly distributed in u. Figures 1–4 show the results obtained in each case. The values of Q are represented in colours and the values are indicated in the colour scale in the right bar of the figures. For each pair MWT, SL, the values of Q have been calculated as the minimum values such that $P(T \leq MWT) = SL$.

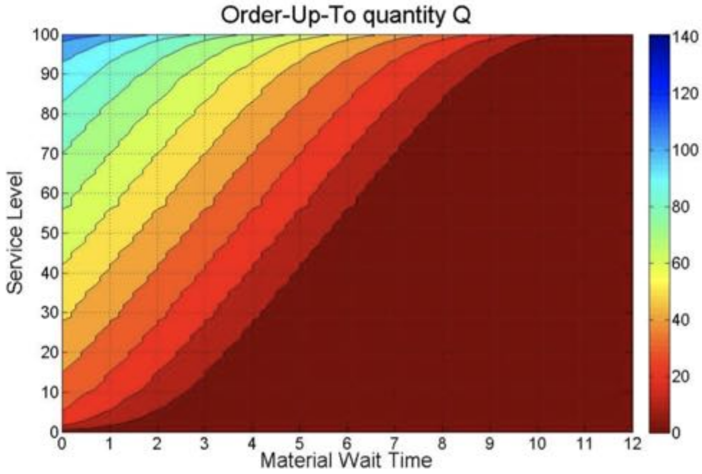

Figure 1: Q as a function of MWT and SL for a system with normal distributed daily demand with $\mu_d = 10$, $\sigma_d = 2$ and lead time with $\mu_l = 3$, $\sigma_l = 1$.

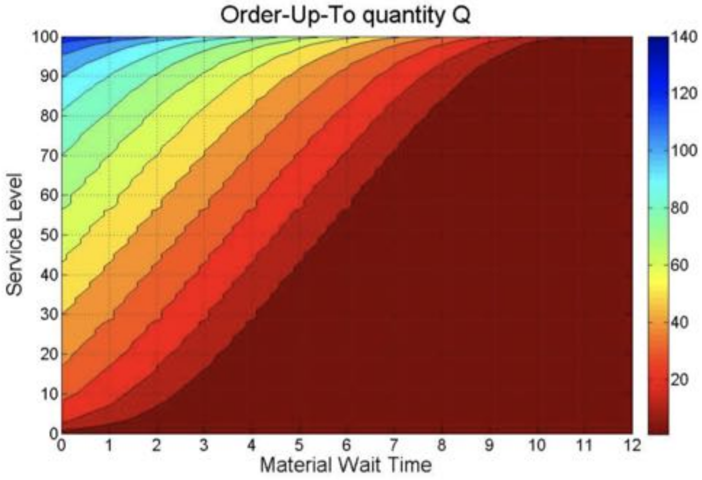

Figure 2: Q as a function of MWT and SL for a system with normal distributed daily demand with $\mu_d = 10$, $\sigma_d = 5$ and lead time with $\mu_l = 3$, $\sigma_l = 1$.

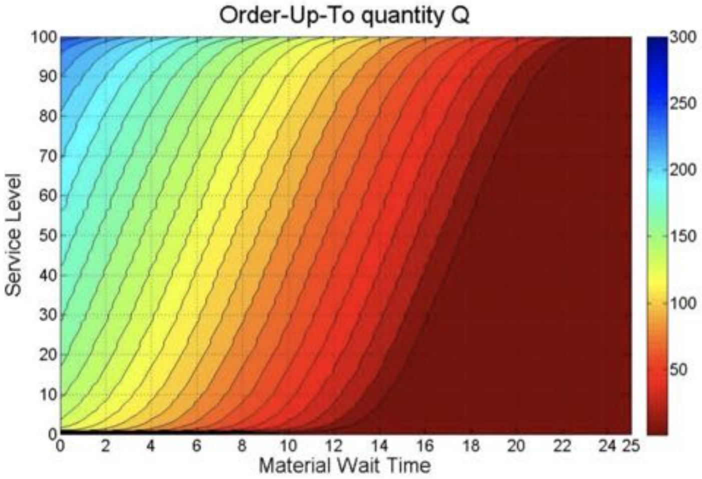

Figure 3: Q as a function of MWT and SL for a system with normal distributed daily demand with $\mu_d = 10$, $\sigma_d = 2$ and lead time with $\mu_l = 15$, $\sigma_l = \sqrt{2}$.

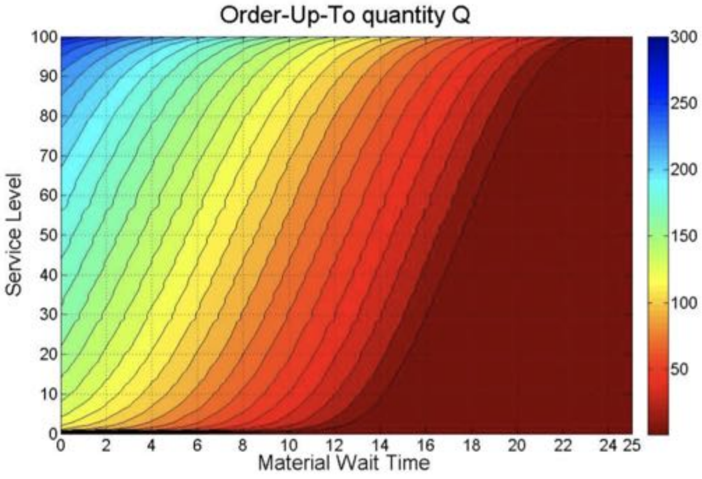

Figure 4: Q as a function of MWT and SL for a system with normal distributed daily demand with $\mu_d = 10$, $\sigma_d = 5$ and lead time with $\mu_l = 15$, $\sigma_l = \sqrt{2}$.

Participants

Maria Aguareles	Universitat de Girona
Unai Aldasoro	Basque Center for Applied Mathematics
Revathi Bacsa	Laboratoire de Chimie de Coordination du CNRS
Wolfgang Bacsa	Université Paul Sabatier
Xavier Bardina	Universitat Autonòma de Barcelona
Carles Barril	Centre de Recerca Matemàtica
Ernest Benedito	Universitat Politècnica de Catalunya
Dusan Bikov	Goce Delcev University
Pere Boqué	Mossos d'Esquadra de Catalunya
Alejandra Cabaña	Universitat Autonòma de Barcelona
Juan Calvo	Universitat Pompeu Fabra
Marc Calvo	Universitat Politècnica de Catalunya
Marta Canadell	Brown University
Marta Casas	Mossos d'Esquadra de Catalunya
Jordi Castro	Universitat Politècnica de Catalunya
Gemma Colldeforns	Centre de Recerca Matemàtica
Enric Costa	Centre de Recerca Matemàtica
Vincent Cregan	Centre de Recerca Matemàtica
Roberto de la Cruz	Centre de Recerca Matemàtica
Carlos Domingo	Universitat de Barcelona
Mario Fernández	Basque Center for Applied Mathematics
Sonia Fernández-Méndez	Universitat Politècnica de Catalunya
Jesús Fernández-Sánchez	Universitat Politècnica de Catalunya
Brendan James Florio	Limerick University
Núria Folguera	Centre de Recerca Matemàtica
Francesc Font	Limerick University
Neus Gómez	Institut Català de Nanociència i Nanotecnologia
Àlex Haro	Universitat de Barcelona
Joan Jané	HP
Giorgi Khimshiashvili	Ilia State University
Andrei Korobeinikov	Centre de Recerca Matemàtica
Antonio Marquina	Universitat de València
Fernando Martínez	Universitat Politècnica de Catalunya
Isabel Moreno	Centre de Recerca Matemàtica
Iain Moyles	Limerick University
Xavier Muñoz	Universitat Politècnica de Catalunya
Tim Myers	Centre de Recerca Matemàtica
Anel Nurtay	Centre de Recerca Matemàtica
Joaquim Ortega	Universitat de Barcelona

Marta Pellicer	Universitat de Girona
Jordi Piella	Institut Català de Nanociència i Nanotecnologia
David Portabella	Universitat de Barcelona
Alfredo Portone	Fusion for Energy
Pere Puig	Universitat Autonòma de Barcelona
Helena Ribera	Centre de Recerca Matemàtica
Jordi Ripoll	Universitat de Girona
Miguel Romero	Universitat de Barcelona
Simone Rusconi	Basque Center for Applied Mathematics
Jordi Saludes	Universitat Politècnica de Catalunya
Susana Serna	Universitat Autònoma de Barcelona
Isabel Serra	Centre de Recerca Matemàtica
Joan Solà-Morales	Universitat Politècnica de Catalunya
Aleksandra Stojanova	Goce Delcev University
Michael Tsardakas	Heriot-Watt University
Zlatko Varbanov	University of Veliko Turnovo
Carlos Vázquez	Universidade da Coruña
Mariona Vilà	Universitat Politècnica de Catalunya